

Pendant Capsule Elastometry

Jonas Hegemann^a, Sebastian Knoche^a, Simon Egger^b, Maureen Kott^b, Sarah Demand^b, Anja Unverfehrt^b, Heinz Rehage^b, Jan Kierfeld^a

^aPhysics Department, TU Dortmund University, 44221 Dortmund, Germany
^bDepartment of Chemistry, TU Dortmund University, 44221 Dortmund, Germany

Abstract

We provide a C/C++ software for the shape analysis of deflated elastic capsules in a pendant capsule geometry, which is based on an elastic description of the capsule material as a quasi two-dimensional elastic membrane using shell theory. Pendant capsule elastometry provides a new in-situ and non-contact method for interfacial rheology of elastic capsules that goes beyond determination of the Gibbs- or dilational modulus from area-dependent measurements of the surface tension using pendant drop tensiometry, which can only give a rough estimate of the elastic capsule properties as they are based on a purely liquid interface model. Given an elastic model of the capsule membrane, pendant capsule elastometry determines optimal elastic moduli by fitting numerically generated axisymmetric shapes optimally to an experimental image. For each digitized image of a deflated capsule elastic moduli can be determined, if another image of its undeformed reference shape is provided. Within this paper, we focus on nonlinear Hookean elasticity because of its low computational cost its wide applicability, but also discuss and implement alternative constitutive laws. For Hookean elasticity, Young's surface modulus (or, alternatively, area compression modulus) and Poisson's ratio are determined; for Mooney-Rivlin elasticity, the Rivlin modulus and a dimensionless shape parameter are determined; for neo-Hookean elasticity, only the Rivlin modulus is determined, using a fixed dimensionless shape parameter. Comparing results for different models we find that nonlinear Hookean elasticity is adequate for most capsules. If series of images are available, these moduli can be evaluated as a function of the capsule volume to analyze hysteresis or aging effects depending on the deformation history or to detect viscoelastic effects for different volume change rates. An additional wrinkling wavelength measurement allows the user to determine the bending modulus, from which the layer thickness can be derived. We verify the method by analyzing several materials, compare the results to available rheological measurements, and review several applications. We make the software available under the GPL license at github.com/jhegemann/opencapsule.

Keywords: microcapsules, elastic capsules, interfacial rheology, capsule shape analysis, wrinkling, Young's surface modulus, Poisson's ratio, bending modulus, pendant drop, tensiometer

1. Introduction

Elastic capsules that consist of a solid thin shell enclosing a liquid volume can be produced artificially by a variety of chemical processes, such as interfacial crosslinking or polymerization [1]. Moreover, solid-like interfaces can form by interfacial adsorption and self-assembly of surface active micro- or nano-particles such as colloidal particles in colloidosomes [2], petroleum [3], various proteins at interfaces [4, 5], for example hydrophobins at water-air interfaces [6]. Eventually, solid-like shells can likewise be formed using layer-by-layer assembly by employing electrostatic interactions of polyelectrolytes [7, 8, 9]. Elastic capsules have many applications for transport and delivery of the enclosed

liquid in pharmaceutical, cosmetic or chemical industry [10]. Likewise, they serve as biological model systems for red blood cells or the cell cortex. For all applications, a characterization of the mechanical properties of the capsule shell, i.e., its elastic moduli, is necessary [11, 10].

Encapsulation applications employ closed microcapsules, but often capsules can likewise be produced in a pendant or hanging capsule geometry, where the capsule is not closed and the capsule edge is attached to a capillary [12, 13, 14, 15, 16, 6, 17, 18, 9]. Such capsules can be produced by self-assembly onto a droplet hanging from a capillary or onto an air bubble rising from a capillary, or by interfacial crosslinking at the interface

of a pendant droplet [19]. An advantage of this pendant capsule geometry is that volume reduction or pressure application can easily be realized by fluid suction through the capillary and it, thus, offers a simple way of micromanipulation for mechanical characterization.

The related pendant droplet tensiometry is a standard tool to determine the surface tension of a liquid interface using the Laplace-Young equation to model the droplet shape [20, 21, 22, 23], which is commercially available. The same Laplace-Young analysis has frequently been applied to pendant elastic capsules with different shell materials or droplets coated with solid-like layers of adsorbed particles [3, 24, 8, 12, 25, 26, 4, 15, 16, 17] resulting in the determination of an “effective surface tension” γ describing the solid shell interface of surface area A . Changing the surface area A in deflation experiments, the so-called Gibbs- or dilational modulus $E_{\text{Gibbs}} = d\gamma/d\ln A$ can be calculated. Pendant drop tensiometry can also be applied to droplets or capsules with a viscoelastic interface by employing oscillating droplets [24, 12, 25, 26, 4]; then a complex dilational modulus can be obtained, which includes a real elastic and an imaginary loss part. The elastic dilational modulus is equal to the area compression modulus K_{2D} for a fluid interface or for a two-dimensional solid interface in a planar Langmuir-Blodgett trough geometry. Application of the same concept to pendant elastic capsules gives misleading results because of inhomogeneous and anisotropic elastic stresses in the capsule geometry and the existence of a curved undeformed reference shape of the capsule [12, 13, 14, 19, 9]. In Ref. [19], an elastic model based on shell theory has been developed which is capable of describing capsule shapes in a deflation experiment more realistically. Similar elastic models have been formulated in Refs. [12, 13, 14, 9]. In Ref. [19] this approach has been extended to the pendant capsule elastometry method, where the elastic model is used to determine two elastic constants, the surface Young modulus Y_{2D} and Poisson’s ratio ν_{2D} , by optimally fitting calculated shapes to experimental images. Pendant capsule elastometry has already been applied to OTS-capsules and hydrophobin-coated bubbles [19] but also to bacterial films at interfaces [27].

Here, we want to present and make publicly available a much more efficient implementation of the pendant capsule elastometry method as a C/C++ software with a high degree of numerical efficiency and automation. In contrast to Ref. [19], where elastic constants were optimized on a grid in parameter space to optimally match the experimental shape profile, we optimize elastic constants in continuous parameter space, which improves both performance and accuracy. Moreover, we

go beyond Ref. [19] and generalize the shape analysis method to other constitutive laws. In particular we investigate the behavior of the shape analysis method in combination with Mooney-Rivlin or neo-Hookean elasticity models, which are commonly used for inextensible polymeric materials.

These significant improvements turn the analysis into a strong tool to investigate different materials in a short time and on a large scale. We demonstrate these capabilities by analyzing a variety of deformation experiments for different materials. In pendant capsule elastometry Young’s modulus and Poisson’s ratio (or the Rivlin modulus and the dimensionless shape parameter) of the two-dimensional capsule shell material are obtained from an analysis of a digitized image of the deflated capsule shape and a second image of its undeformed reference shape. If the capsule wrinkles upon deflation, an additional wrinkling wavelength measurement allows us to determine the bending modulus, from which the layer thickness can be derived if the shell material is a thin layer of a three-dimensional isotropic elastic material.

2. Available experimental methods

Several interfacial rheology methods exist, which allow the determination of the elastic properties of the capsule shell material. We review four different rheological methods, which we will use as references for the pendant capsule method described in this paper. Typical experimental methods are (i) surface shear-rheometry [28], (ii) Langmuir-Blodgett trough, (iii) shear flow rheoscope (flow cell) [29], and (iv) spinning drop apparatus [30]. Methods (i) and (ii) work with *planar* membranes of the shell material, whereas methods (iii) and (iv) directly work in the curved capsule geometry, like pendant capsule elastometry does. Apart from these four methods there are other contact techniques such as probing capsules with AFM tips, micromanipulators, or optical tweezers (see Ref. [10] for a review). Pendant capsule elastometry is a non-contact technique and, in comparison with methods (iii) and (iv), it does not require fluid motion in the surrounding fluid. We focus here on elastic capsule shell materials. For viscoelastic materials there are other interfacial rheology methods available [25], such as double wall ring rheometry [31] or magnetic rod rheometry [32].

In shear-rheometry, a transducer (thin disk or ring) is placed in a circular vessel at a planar liquid-liquid or air-liquid interface; between transducer and container wall a membrane with the shell material is prepared, such

that membrane deformations can be applied in circumferential direction. While oscillating at a certain frequency, the mechanical response is measured, which gives the interfacial storage modulus μ' and the loss modulus μ'' . From μ' one determines the surface Young modulus $Y_{2D} = 2(1 + \nu_{2D})\mu'$ provided that the Poisson ratio ν_{2D} is known.

In a Langmuir-Blodgett trough, a membrane made from the shell material is prepared in a rectangular vessel at a liquid-liquid or air-liquid interface. During compression of the membrane, the surface tension γ and area A are measured, from which the Gibbs modulus $E_{\text{Gibbs}} = d\gamma/d\ln A$ is determined. The Gibbs modulus E_{Gibbs} corresponds to the area compression modulus K_{2D} in the planar trough geometry; we will show that these two parameters differ substantially in the curved capsule geometry.

In a shear flow rheoscope, a closed capsule is placed in a liquid phase between two concentric hollow cylinders. By rotating the cylinders in opposite directions a shear flow is induced, which deforms the capsule. Comparing the shape profile with ellipses gives the compression of the surface and, thus, the surface Young modulus [33].

In a spinning drop apparatus a closed capsule is placed in a cylindrical vessel filled with a fluid. When the vessel is rotated at high frequencies the capsule is exposed to centrifugal forces, which induce a deformation. Similar to the shear flow rheoscope the surface Young modulus is obtained from a shape analysis [30].

3. Pendant capsule elastometry

The pendant drop apparatus is widely spread in industrial environments and research departments. Typically it is shipped with a software performing a Laplace-Young analysis on captured images in order to determine the surface tension of fluid interfaces. In this paper, we provide a generalized algorithm as a C/C++ software, which is able to perform an analogous shape analysis for elastic membranes in order to determine the surface Young modulus Y_{2D} and the Poisson ratio ν_{2D} (or the Rivlin modulus Y_M and the dimensionless shape parameter Ψ) of the material. In section 9, we will present examples with several different capsule shell materials, which demonstrate that our software is widely applicable and that pendant capsule elastometry results are in good agreement with other rheological measurements. As compared to pendant drop tensiometry, the shape analysis of pendant elastic capsules comes at the cost of an additional amount of runtime (one or

few minutes per image), but enables the proper characterization of the elastic material properties of capsules.

In the following we will focus on pendant elastic capsules produced by interfacial crosslinking, gelation or polymerization, see Fig. 1. Consider a droplet of size $\sim 1\text{mm}$ hanging from a capillary. The inner (liquid) and outer phase (liquid/air) are separated by a liquid interface with a surface tension compensating the pressure difference. Surfactants, and potentially crosslinkers, are dissolved in the droplet or the surrounding fluid. When forming the droplet, surfactants immediately start to adsorb to the interface and spread over it. During equilibration of bulk and interface surfactant concentrations, the surface tension decreases. Though the interface is now partially occupied by surfactants, it is still a liquid interface obeying the Laplace-Young law. This changes when crosslinkers start to connect previously freely diffusing surfactants and turn the interface into an elastic solid by forming elastic bonds above a threshold concentration for gelation. After completion of this crosslinking process, an elastic capsule in its reference, i.e., undeformed or stress-free shape has been formed.

By slowly reducing the volume of the capsule one observes elastic deformations, which are specific to the microscopic structure of the membrane. We neglect such microscopic details by assuming a homogeneous isotropic material and focus on the set of elastic constants, which describe the macroscopic properties of the membrane. Nonetheless, microscopic effects can be observed in the elastic constants, if these are measured during the course of deflation. Phase transitions that occur as a function of the accessible surface area induce a rapid change in the elastic moduli and are, therefore, detected. Viscoelastic or creep behavior are detected, if elastic moduli change with the rate of volume reduction. Aging effects are detected, if elastic moduli change during the course of multiple cycles of de- and inflation that are applied to the capsule.

The general aim of pendant capsule elastometry is the same as in pendant drop tensiometry, namely to adjust material parameters (elastic constants or surface tension and, eventually, pressure) such that theoretically generated axisymmetric capsule/droplet shapes optimally fit a given experimental shape. The shape of an elastic capsule can be described by classical elastic shell theory (if bending moments are included) or elastic membrane theory (if bending moments are neglected) [34], which requires an elastic material model specified by its constitutive stress-strain relation or a corresponding elastic energy. We neglect bending moments and mainly focus on Hookean membrane elasticity throughout this paper but also discuss Mooney-Rivlin or neo-Hookean

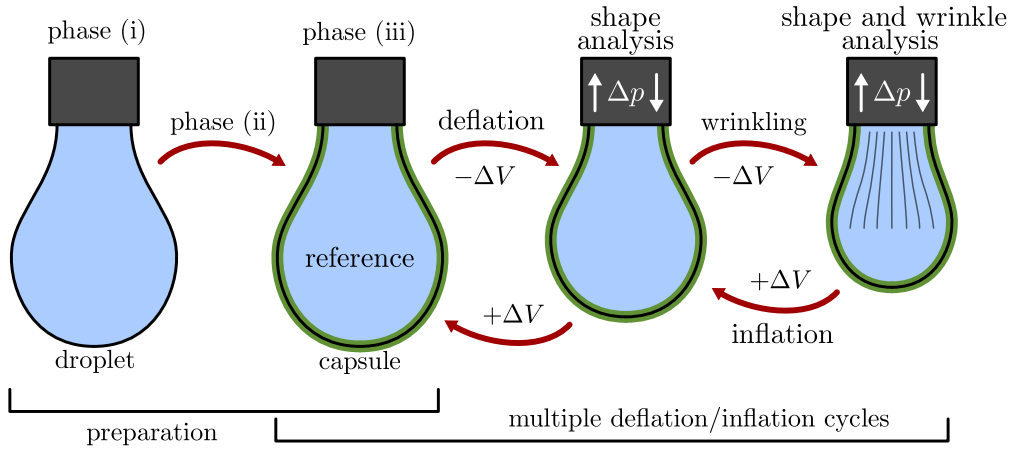


Figure 1: Typical experimental procedure in pendant drop elastometry. In a first step, a pendant capsule is prepared by coating a pendant droplet with an elastic shell, for example, by interfacial crosslinking. When the coating process is completed, cyclic pressure/volume changes are applied to the capsule and images are taken continuously during this procedure. Fitting theoretical shapes from the elastic model to the shape profile extracted from the image gives the elastic moduli of the shell membrane. For sufficiently solid and thin materials wrinkles occur upon deflation, which can be analyzed to give the bending modulus of the shell membrane. The procedure allows for multiple inflation-deflation-cycles, which can reveal aging effects or hysteresis. Application of different volume change rates can reveal viscoelastic effects.

elastic membranes, which are also implemented in the software. Each elastic material model is characterized by a set of elastic material parameters, such as the surface Young modulus Y_{2D} and the Poisson ratio ν_{2D} in Hookean membrane elasticity (or the Rivlin modulus Y_M and the dimensionless shape parameter Ψ in Mooney-Rivlin membrane elasticity), which we aim to determine by optimally fitting theoretical to experimental shapes. For an elastic material we also need an elastically relaxed reference shape, with respect to which local stretch factors or strains in the material are defined, in order to calculate deformed shapes. This problem will be discussed in Sec. 5 in detail.

In a pendant capsule geometry (see Fig. 1) the capsule is formed hanging from an axisymmetric capillary. Therefore, we assume axisymmetric shapes which can be uniquely described by their shape profile, i.e., the intersection of the capsule surface with a plane. We use cylindrical coordinates to describe axisymmetric shapes (with the z -axis as symmetry axis) and describe the profile as contour in the r - z -plane, see Fig. 2. The shape profile can be trivially acquired experimentally by taking a two-dimensional image from the side.

For a given elastic model, tangential and normal force equilibrium of stresses and external forces at every point on the surface determine the equilibrium shape. The equations of force equilibrium, geometric relations, and constitutive relations can be used to derive a closed sys-

tem of first order differential equations for r , z , a slope angle ψ (see Fig. 2) and the meridional elastic stress τ_s with the arc length s_0 of the undeformed spherical profile as independent variable, which are called shape equations and discussed below in Sec. 4 in detail. The shape equations use the constitutive relations and are, therefore, specific for the elastic model that is used to describe the capsule material. We discuss shape equations for Hookean elasticity, Mooney-Rivlin, and neo-Hookean materials in detail in Sec. 4. The solution of the shape equations determines the theoretical shape profile of an axisymmetric shape for a given set of material parameters, a given pressure inside the capsule, and a given elastically relaxed reference shape. We solve the shape equations numerically by a shooting method (see Appendix C) because boundary conditions have to be applied at both ends of the shape profile, i.e., at the attachment point to the capillary and at the lower apex of the capsule.

Comparison between experiment and theory is achieved by overlaying the theoretical shape and the image, regardless of the employed elastic model. In pendant capsule elastometry elastic material parameters of individual capsules are then determined by fitting the parameters (i.e., elastic moduli) of the model until the theoretical shape (for each parameter set obtained by solution of the shape equations) optimally matches the contour given in the image. We determine the optimal

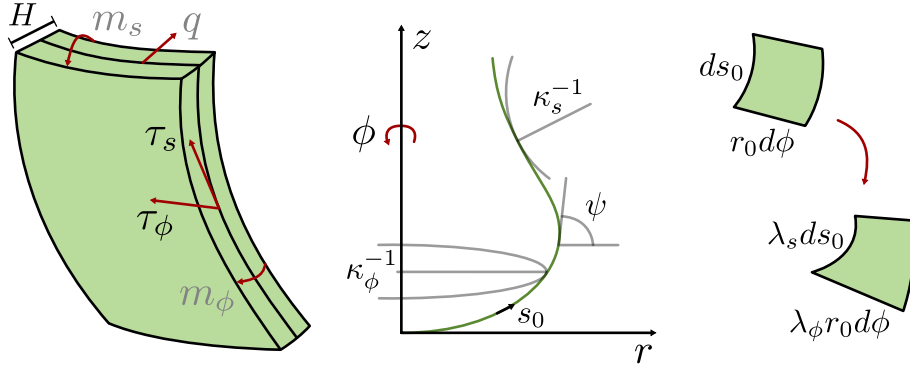


Figure 2: Parametrization of the shape equations. Axisymmetric shapes are described by a shape profile in the r - z -plane, which generates a surface of revolution by rotation with respect to the z -axis. The shape equations are integrated over the thickness H of an infinitesimal membrane patch, which is an approximation for thin shells. Forces and torques resulting from curvature are neglected and, thus, depicted in gray.

fit by minimizing the mean-square deviations between image contour points and theoretical contour (see Appendix D).

This approach works with different constitutive relations with different numbers of elastic moduli, as long as the shape is sensitive to each of the employed material parameters. One prominent example for a parameter, where the shape is rather insensitive to, is the bending modulus E_B for a thin capsule membrane. Therefore, the bending modulus of a thin capsule membrane cannot be determined reliably by fitting to the shape profiles but has to be determined via a different approach, namely the analysis of wrinkle wavelengths. In case of a wrinkling instability, we have to use an effective constitutive relation in the wrinkled part of the shape profile and corresponding effective shape equations, which are also discussed in the next Sec. 4.

Thus, for the complete pendant elastometry shape analysis we have to handle three major tasks, (i) solving the shape equations for the given elastic model to determine the theoretical deformed shape from the elastically relaxed reference shape, (ii) decoding the contour from the image and (iii) adapting the model parameters (elastic moduli) to fit the contour. Details of the algorithm are described in the Appendix: (i) solving the shape equations by a multiple shooting method in Appendix C and determining the reference shape in Appendix B, (ii) the image processing in Appendix F, and (iii) parameter determination by shape regression in Appendix D. In contrast to previous implementations [19], we strongly focus on numerical performance and robustness as well as a high degree of automation and make the resulting C/C++ code publicly available under

a GPL License [35]. We also implement shape equations for different constitutive relations for elastic membranes: nonlinear Hookean as in Ref. [19], strictly linear Hookean as in Ref. [12, 14, 9], Mooney-Rivlin, and neo-Hookean membranes as in Ref. [13]. We verify our method by analyzing several materials and comparing the results to rheological measurements.

4. Shape equations

4.1. Liquid reference shape

The shape of a liquid droplet hanging from a capillary can be described by a system of nonlinear differential shape equations with the arc length s_0 of the contour as independent variable,

$$\begin{aligned} r'_0(s_0) &= \cos \psi_0, & z'_0(s_0) &= \sin \psi_0, \\ \psi'_0(s_0) &= (p_0 - \Delta \rho g z_0) / \gamma - \sin \psi_0 / r_0 \end{aligned} \quad (1)$$

(primes denote derivatives d/ds_0). The z_0 -axis is the axis of symmetry, r_0 the radius and ψ_0 the slope angle of the contour. We use quantities with a subscript “0” because we will employ a Laplace-Young fit for the elastically relaxed reference state of our elastic capsule before deformation by volume reduction, see Sec. 5 below. The first two equations are geometric relations involving the slope angle ψ_0 ; the third equation is the Laplace-Young force balance equation in cylindrical parametrization, where we use $\kappa = d\psi_0/ds_0$ for the curvature of the droplet. Note that the Laplace-Young shape equations (1) are already closed, i.e., the right hand side is completely written in terms of the three functions $r_0(s_0)$, $z_0(s_0)$, $\psi_0(s_0)$ on the left hand side. The

arc length s_0 varies in the range $[0, L_0]$; the lower apex is located at $s_0 = 0$ the drop is attached to the capillary at $s_0 = L_0$. The Laplace-Young shape equations are solved with initial conditions $r_0(0) = 0$, $\psi_0(0) = 0$, and $z_0(0) = \zeta$ arbitrary; the contour length L_0 is determined by the boundary condition $r_0(L_0) = a/2$, where a is the inner capillary diameter. The right hand side of $\psi'_0(0)$ at $s_0 = 0$ is ambiguous using the initial values; L'Hôpital's rule leads to $\psi'_0(0) = (p_0 - \Delta\rho g\zeta)/2\gamma$ at $s_0 = 0$ which is also needed to start the integration of the shape equations. The solution gives the droplet shape $(r_0(s_0), z_0(s_0))$ as a function of the parameters p_0 , $\Delta\rho$ and γ . The pressure p_0 is the hydrostatic pressure at the apex (if $\zeta = 0$), $\Delta\rho$ the density difference between the inner and outer phase, and γ the surface tension. The pressure difference $\Delta\rho g z_0$ is induced by gravity.

4.2. Elastic membrane materials

The Laplace-Young shape equations (1) are well suited for fluid interfaces, but interfacial crosslinking or gelation actually turns the interface into a two-dimensional elastic solid. From classical shell theory and neglecting bending moments one derives the elastic shape equations with the arc length s_0 of the *undeformed* spherical contour as independent variable, [19]

$$\begin{aligned} r'(s_0) &= \lambda_s \cos \psi, & z'(s_0) &= \lambda_s \sin \psi, \\ \psi'(s_0) &= \frac{\lambda_s}{\tau_s} \left(p - \Delta\rho g z - \frac{\sin \psi}{r} \tau_\phi \right), \\ \tau'_s(s_0) &= -\lambda_s \frac{\cos \psi}{r} (\tau_s - \tau_\phi) \end{aligned} \quad (2)$$

(primes denote derivatives d/ds_0). The meridional and hoop stretches $\lambda_s = ds/ds_0$ and $\lambda_\phi = r/r_0$ capture the elastic deformation state and are, thus, only defined with respect to the undeformed reference shape $r_0(s_0)$ (with subscript "0"); the corresponding strains are $(\lambda_s^2 - 1)/2 \approx \lambda_s - 1$ and $(\lambda_\phi^2 - 1)/2 \approx \lambda_\phi - 1$. Note that s denotes the arc length of the deformed configuration, whereas s_0 denotes the arc length of the undeformed configuration. Fig. 2 illustrates the involved quantities. The first two equations are geometric relations involving the slope angle ψ . The third and fourth equations describe normal and tangential force balance, respectively. In the normal force balance, the principal curvatures $\kappa_s = d\psi/ds$ and $\kappa_\phi = \sin \psi/r$ have been used.

It is important to note that eqs. (2) are still valid regardless of the constitutive relation. This is also the reason why eqs. (2) are not yet closed: we have to rearrange the constitutive relations $\tau_s = \tau_s(\lambda_s, \lambda_\phi)$ and $\tau_\phi = \tau_\phi(\lambda_s, \lambda_\phi)$ in order to express τ_ϕ and λ_s on the right hand side of eqs. (2) in terms of τ_s and $\lambda_\phi = r/r_0$, i.e.,

in terms of the functions $\tau_s(s_0)$ and $r(s_0)$ from the left hand side (and the known reference shape $r_0(s_0)$). We will discuss closure of the shape equations for different constitutive relations and also in the presence of wrinkles in the following sections. Once the shape equations (2) are closed, they are solved with the boundary conditions $r(0) = 0$, $\psi(0) = 0$, and $z(0) = \zeta$ arbitrary at the capsule apex. A fourth boundary condition $\tau_s(0) = \mu$ at the capsule apex serves as shooting parameter to satisfy the boundary condition $r(L_0) = a/2$ at the capillary (see Appendix C for the numerical realization of the shooting method). The right hand sides of $\psi'(0)$ and $\tau'_s(0)$ at $s_0 = 0$ are ambiguous using the initial values; L'Hôpital's rule leads to $\lambda_s(0) = \lambda_\phi(0)$ and isotropic tensions $\tau_s(0) = \tau_\phi(0)$ at the apex. This results in $\tau'_s(0) = 0$ and $\psi'_0(0) = \lambda_s(0)(p - \Delta\rho g\zeta)/2\mu$ at $s_0 = 0$ which are also needed to start the integration.

The pressure p is the hydrostatic pressure at the apex of the deflated shape (if $\zeta = 0$), which is below the pressure p_0 of the reference shape, i.e., $p < p_0$. In principle, information on the pressure p could be experimentally available if pressure measurements are possible. In the current implementation of the method and all applications below, the pressure p serves as Lagrange multiplier that is changed to control the capsule volume and determined from shape fitting along with the elastic moduli.

4.3. Nonlinear Hookean elastic membrane

For a Hookean stretching elasticity the meridional and circumferential tensions τ_s and τ_ϕ are related to the stretches λ_s and λ_ϕ by the constitutive relations

$$\begin{aligned} \tau_s &= \frac{1}{\lambda_\phi} \frac{Y_{2D}}{1 - \nu_{2D}^2} ((\lambda_s - 1) + \nu_{2D}(\lambda_\phi - 1)) + \gamma, \\ \tau_\phi &= \frac{1}{\lambda_s} \frac{Y_{2D}}{1 - \nu_{2D}^2} ((\lambda_\phi - 1) + \nu_{2D}(\lambda_s - 1)) + \gamma, \end{aligned} \quad (3)$$

where Y_{2D} is the surface Young modulus and ν_{2D} Poisson's ratio. Instead of the surface Young modulus Y_{2D} we could also use the surface shear modulus μ' (sometimes called storage modulus G') or the area compression modulus K_{2D} as alternative elastic constants of the membrane material, which are related by

$$\mu' = \frac{Y_{2D}}{2(1 + \nu_{2D})} = K_{2D} \frac{1 - \nu_{2D}}{1 + \nu_{2D}}, \quad K_{2D} = \frac{Y_{2D}}{2(1 - \nu_{2D})}. \quad (4)$$

Although we use a simple Hookean elastic energy, the relations (3) are *nonlinear* because of the additional $1/\lambda$ -factors, which arise for purely geometrical reasons: the Hookean elastic energy density is defined per undeformed unit area, whereas the Cauchy stresses τ_s and τ_ϕ

are defined per deformed unit length. The relations (3) still contain an interfacial tension γ because the elastic capsule is formed in the initial shape of a fluid interface. We assume that γ is the tension of the fluid interface in presence of a saturated interfacial surfactant concentration before crosslinking the surfactants to an elastic shell. This assumption is addressed in detail in Sec. 5.

The system of shape equations (2) can now be closed by using on the right hand side the constitutive relation for τ_ϕ from eqs. (3), and the relation

$$\lambda_s = (1 - \nu_{2D}^2) \lambda_\phi \frac{\tau_s - \gamma}{Y_{2D}} - \nu_{2D}(\lambda_\phi - 1) + 1 \quad \text{with} \quad \lambda_\phi = \frac{r}{r_0}, \quad (5)$$

which derives from the constitutive relation for τ_s from eqs. (3). The resulting shape equations have also been used in Ref. [19].

4.4. Strictly linear Hookean, Mooney-Rivlin, and neo-Hookean membranes

At this point we want to compare to similar approaches to pendant capsule shapes by shape equations in the literature. Shape equations very similar to eqs. (2) have been obtained in Refs. [12, 13, 14, 9], where the same normal and tangential force balance and geometry relations have been employed, however, in combination with different constitutive relations. In Ref. [13], an incompressible neo-Hookean constitutive relation has been used for the shell material, which is a special case of an incompressible Mooney-Rivlin material. In Refs. [12, 14, 9], a strictly linear Hookean constitutive law has been used, where the $1/\lambda$ -factors are missing as compared to the relations (3), (note that constitutive linear Hookean laws in Refs. [14, 9] contain some misprints). In Refs. [13, 14], exemplary theoretical shapes have been discussed but no elastic parameters have been determined from systematically fitting theoretical shapes to experimental images, i.e., using a least square minimization algorithm to optimally match the experimental shape with a theoretically generated contour. Therefore, we want to discuss how the shape equations (2) can be closed not only for a *nonlinear Hookean membrane* as in (5) but also for other constitutive relations.

The simplest example is a *strictly linear Hookean membrane*, where the closure is simply lacking one factor λ_ϕ as compared to eq. (5) [36],

$$\lambda_s = (1 - \nu_{2D}^2) \frac{\tau_s - \gamma}{Y_{2D}} - \nu_{2D}(\lambda_\phi - 1) + 1 \quad \text{with} \quad \lambda_\phi = \frac{r}{r_0}. \quad (6)$$

Thus, the closure relations are, as for the nonlinear Hookean membrane, analytically accessible.

The *Mooney-Rivlin membrane model* is frequently used for polymer materials as it describes membranes made from incompressible materials. It describes these materials also deep into the nonlinear regime as it captures effects from strain-stiffening. It has the constitutive relation [36]

$$\begin{aligned} \tau_s &= \frac{Y_M}{3\lambda_\phi\lambda_s} \left(\lambda_s^2 - \frac{1}{(\lambda_s\lambda_\phi)^2} \right) [\Psi + (1 - \Psi)\lambda_\phi^2] + \gamma, \\ \tau_\phi &= \frac{Y_M}{3\lambda_\phi\lambda_s} \left(\lambda_\phi^2 - \frac{1}{(\lambda_s\lambda_\phi)^2} \right) [\Psi + (1 - \Psi)\lambda_s^2] + \gamma, \end{aligned} \quad (7)$$

where Y_M is the surface Rivlin modulus and Ψ a dimensionless shape parameter. A *neo-Hookean membrane* has $\Psi = 1$. In the limit of small stretches a neo-Hookean membrane reduces to a Hookean membrane with $Y_{2D} = Y_M$ and $\nu_{2D} = \nu_{3D} = 1/2$ (for incompressibility). In order to close the shape equations we have to use the constitutive relations (7) to find λ_s and τ_ϕ as a function of τ_s and $\lambda_\phi = r/r_0$ in order to replace λ_s and τ_ϕ on the right hand side in the shape equations (2), as for the Hookean case. Unfortunately, this involves roots of fourth order polynomials. Therefore, we perform this task numerically in our software. Note that this numerical solution has to be obtained in each step of numerical integration of the shape equations, i.e., during each evaluation of the shape equations, which increases the computational runtime significantly (roughly by a factor of 10) as compared to fits with the nonlinear Hookean relation.

4.5. Wrinkling

The above shape equations (2) only hold for thin materials $H \ll R$, since we neglected bending elastic energy terms resulting from curvature, which can, in principle, be included into shape equations (see Ref. [37]). This is justified as the bending modulus is expected to scale $E_B \propto H^3$, whereas Young's modulus scales as $Y_{2D} \propto H$. Consequently, for thin capsule shells, the shape profiles are insensitive to changes in the bending modulus, which makes it practically impossible to infer E_B from fitting theoretical shape contours to experimental images.

Nevertheless, we can determine the bending modulus in a separate analysis of the wrinkle wavelength [19]. Wrinkles in meridional direction are present if $\tau_\phi < 0$, i.e., if compressive stresses occur in circumferential direction (neglecting a small critical Euler stress necessary to trigger wrinkling). This condition determines the extent of the wrinkled region in meridional direction. In

order to describe wrinkled shapes violating axisymmetry we use a pseudo-surface $(\bar{r}(s_0), z(s_0))$ (all modified quantities related to the pseudo-surface are denoted with bars) representing the average amplitude of the wrinkling modulation. If $\tau_\phi < 0$, the algorithm switches to a different set of shape equations for the pseudo-surface which is obtained by explicitly setting $\tau_\phi = 0$ [19]. The modified set of shape equations is also obtained from force-balance for the pseudo-surface. The meridional stresses for the pseudo-surface are related to the original stresses by $\bar{\tau}_s = \tau_s \lambda_\phi / \bar{\lambda}_\phi$, where $\bar{\lambda}_\phi = \bar{r}/r_0$ is the apparent stretch of the pseudo-surface. Together with $\bar{\tau}_\phi = \tau_\phi = 0$ we obtain shape equations for the pseudo-surface,

$$\begin{aligned}\bar{r}'(s_0) &= \lambda_s \cos \bar{\psi}, & z'(s_0) &= \lambda_s \sin \psi, \\ \bar{\psi}'(s_0) &= \frac{\lambda_s}{\bar{\tau}_s} (p - \Delta \rho g z), \\ \bar{\tau}'_s(s_0) &= -\lambda_s \frac{\cos \bar{\psi}}{\bar{r}} \bar{\tau}_s.\end{aligned}\quad (8)$$

Note that these shape equations hold independently of the constitutive relation of the material. Therefore, they are not yet closed. To close these shape equations we need to rearrange the constitutive relations $\bar{\tau}_s = \tau_s(\lambda_s, \lambda_\phi) \lambda_\phi / \bar{\lambda}_\phi$ of the considered model and the wrinkling condition $0 = \tau_\phi(\lambda_s, \lambda_\phi)$ in order to express λ_s in terms of $\bar{\tau}_s$ and $\bar{\lambda}_\phi = \bar{r}/r_0$. We switch to this new set of shape equations (8) as soon as $\tau_\phi < 0$ is reached at $s_0 = s_1$ along the contour; this gives a switching condition that also depends on the constitutive relation of the material. We switch back to the shape equations (2) without wrinkles as soon as this condition is violated again at $s_0 = s_2 > s_1$. The extent of the wrinkled region is $L_w = s_2 - s_1$.

For a nonlinear Hookean membrane the constitutive relations (3) lead to a wrinkling condition

$$\lambda_\phi = 1 - \gamma \frac{1 - \nu_{2D}^2}{Y_{2D}} \lambda_s - \nu_{2D}(\lambda_s - 1) \quad (9)$$

which is also used to identify the wrinkled region $\tau_\phi < 0$ along the contour. The constitutive relations (3) also lead to the following expression for λ_s in terms of $\bar{\tau}_s$ and $\bar{\lambda}_\phi = \bar{r}/r_0$,

$$\lambda_s = \frac{\bar{\lambda}_\phi \bar{\tau}_s + Y_{2D} - \gamma(1 + \nu_{2D})}{Y_{2D}(1 - 2\nu_{2D}) - (1 - \nu_{2D}^2)\gamma^2/Y_{2D}}, \quad (10)$$

which closes the modified shape equations (8) in the wrinkled region.

Similarly we proceed for the constitutive relations of a strictly linear Hookean, and eqs. (7) of a Mooney-

Rivlin or neo-Hookean membrane in the wrinkled region. For the strictly linear Hookean membrane the wrinkling condition $\tau_\phi = 0$ is given by

$$\lambda_\phi = 1 - \gamma \frac{1 - \nu_{2D}^2}{Y_{2D}} - \nu_{2D}(\lambda_s - 1), \quad (11)$$

where a factor λ_s is missing compared to (9). Again, we find a relation for the meridional stretching factor in terms of $\bar{\tau}_s$ and $\bar{\lambda}_\phi = \bar{r}/r_0$,

$$\begin{aligned}\lambda_s &= \frac{Y_{2D}(Y_{2D} + \gamma(\nu - 1))(1 + 2\nu)}{2Y_{2D}^2\nu} \\ &\pm \frac{\sqrt{Y_{2D}^2(Y_{2D}^2 + \gamma^2(\nu - 1)^2 + 2Y_{2D}(\gamma(\nu - 1) - 2\bar{\lambda}_\phi\bar{\tau}_s\nu))}}{2Y_{2D}^2\nu},\end{aligned}\quad (12)$$

where the solution with the negative root has to be chosen.

Unfortunately, for the Mooney-Rivlin membrane analytic expressions are impracticable since they contain roots of fourth order polynomials. However, λ_s and λ_ϕ can be reliably determined by numerically solving

$$\tau_\phi(\lambda_s, \lambda_\phi) = 0 \quad \text{and} \quad \bar{\tau}_s - \tau_s(\lambda_s, \lambda_\phi) \lambda_\phi / \bar{\lambda}_\phi = 0. \quad (13)$$

Note that, in the wrinkled region, λ_s and λ_ϕ have to be determined, whereas in the non-wrinkled region λ_s and τ_ϕ have to be determined. The solution $(\lambda_s, \lambda_\phi)$ of the above set of equations closes the shape equations (8) and can, in principle, be obtained in the same way for any constitutive law.

The extent of the wrinkled region where $\tau_\phi < 0$ of course depends on the value of the interfacial tension γ in all constitutive relations (3) or (7). The fact that we generally obtain good agreement with experiments regarding the extent of the wrinkled region also supports the inclusion of the interfacial tension into the constitutive relations.

5. Equilibrium and reference shapes

Solutions of the elastic shape equations (2) presume an elastically relaxed reference shape, with respect to which elastic strains are defined. The choice of the reference shape is subject to certain assumptions which will be discussed in this section.

Capsule formation by crosslinking or polymerization proceeds via three phases (see Fig. 1). In phase (i) we have a liquid drop without any surfactants and a stationary shape (which is a teardrop shape due to gravity). Phase (ii) starts when surfactants and/or crosslinkers are

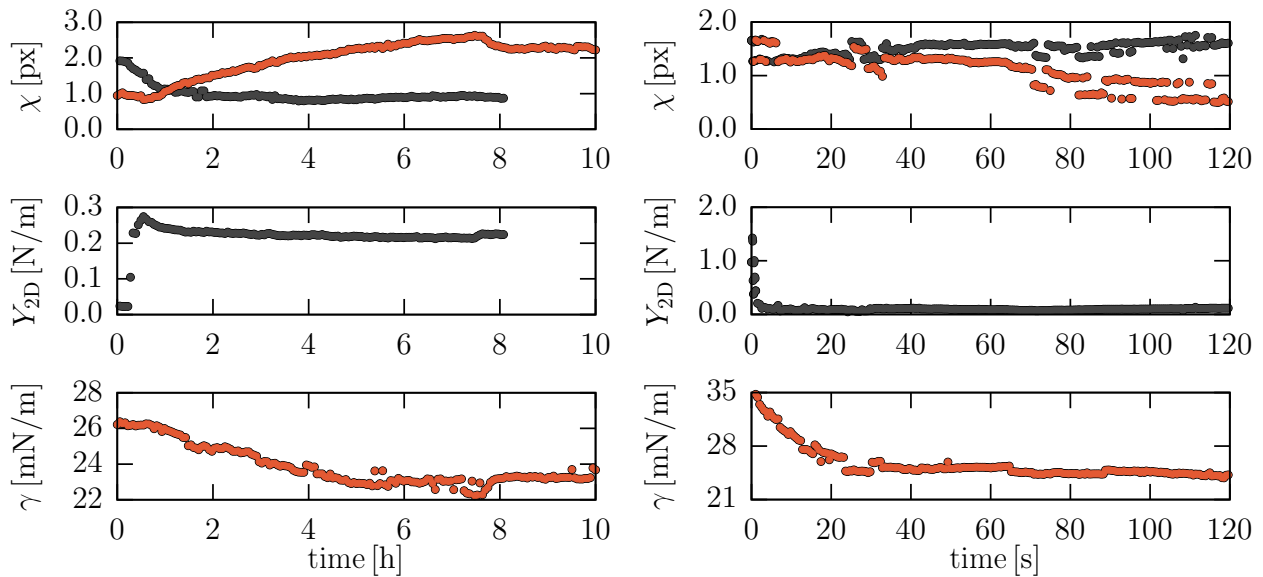


Figure 3: The interfacial gelation phase (ii) fitted with a model for liquid interfaces (Laplace-Young, orange) and a model for elastic interfaces (Hooke membrane, gray), where we use the reference shape from the very beginning of phase (ii), i.e., phase (i). No active pressure or volume change have been applied. **Left:** H₂O-droplet coated with Ce(SO₄)₂ and CTAB-surfactants in a dodecane phase. **Right:** OTS-capsule, i.e., a *p*-xylyol droplet in solution with 1,2,4-trichlorobenzene and coated with OTS in a glycerol-water mixture.

added to one of the bulk phases such that adsorption of surfactants and subsequent crosslinking into a two-dimensional network can occur. If surfactants and/or crosslinkers are dissolved in the droplet or the surrounding fluid, then phase (ii) starts immediately when forming the droplet. In phase (ii) the shape changes and the capsule finally reaches a new equilibrium shape. In phase (iii) the capsule is in its new stationary shape after successful crosslinking; this is the state where the deflation experiment is started.

For the regression of deflated capsule shapes we usually assume that the equilibrium state reached in phase (iii) is identical to the elastically relaxed state and, thus, free of elastic tensions. As discussed above, we also assume in the constitutive relations (3) that the surface tension γ gives a constant contribution to the tensions τ_s and τ_ϕ . Then the surface stress in the elastically relaxed state of the membrane is solely determined by the isotropic surface tension γ . We thus assume in (3) that the elastically relaxed state can be described as a liquid drop shape using the Laplace-Young equation. Based on these two assumptions we use a Laplace-Young fit for the equilibrium shape in phase (iii).

These two assumptions are based on the following picture for the crosslinking process in phase (ii): When adding surfactants to one of the bulk phases at the beginning of phase (ii), the surface tension typically decreases linearly or exponentially in time until it reaches

a plateau at the equilibrium surface tension γ_A . The actual crosslinking of the membrane only happens *after* the plateau at the surface tension γ_A has been reached. During crosslinking the interfacial tension γ_A of the fluid interface remains unchanged. If this picture is valid, we should observe a sagging of the capsule under the action of gravity while a decreasing surface tension gives shapes that can be successfully fitted using the Laplace-Young shape equations (1). The sagging should stop when the surface tension reaches the plateau. During this plateau phase the crosslinking is established, while the capsule shape is unchanged. Fig. 3 (right) shows an example of an OTS-capsule where all these features can indeed be observed. Fitting the shape using the Laplace-Young shape equations gives only small errors and the interfacial tension γ follows the expected temporal evolution.

There are, however, capsule formation processes which deviate from this picture. Another possible scenario is that the formation of a solid shell by crosslinking happens earlier in phase (ii) but further polymerization during phase (ii) generates elastic strains and stresses. All further shape changes during phase (ii) have to be interpreted as a result of strain and stress generation during the polymerization process, and the capsule shell is pre-stressed in the equilibrium state in phase (iii). Then the elastic reference shape is not exactly known and, in principle, can be any of the shapes

encountered in phase (ii). One extreme assumption is that crosslinking is fast and a solid membrane is established right at the beginning of phase (ii). Then the shape in the beginning of phase (ii) directly after addition of surfactants and crosslinkers can be viewed as the elastic reference shape and all subsequent shapes should be fitted with an elastic model using this reference shape. Fits with the elastic model should reveal how strains, stress, and elastic moduli evolve during phase (ii).

In order to decide which choice of reference shape is most appropriate, one can try different fits using different shapes from phase (ii) as elastically relaxed reference shapes (for example, from the end or the beginning of phase (ii)). All shapes before the reference shape are fitted using the Laplace-Young shape equations and described by an interfacial tension γ that decreases in time. All shapes following the reference shape are fitted using the elastic shape equations and described by a surface Young modulus Y_{2D} and a Poisson ratio ν_{2D} , which evolve in time. The reference shape giving the best fits (with smallest errors) should be chosen. Moreover, choices of reference states producing unphysical results, such as a surface Young modulus Y_{2D} which is decreasing in time during the crosslinking process in phase (ii) (more crosslinks or junction points should always increase Y_{2D}), should be discarded.

Two examples are shown in Fig. 3. OTS-capsules show the typical sagging in phase (ii) and can be fitted quite well with the Laplace-Young shape equations giving a surface tension γ , which at first decreases linearly or exponentially and then reaches a plateau, consistent with the standard scenario that the shell is crosslinked at the end of phase (ii). But the shapes can also be fitted quite well assuming that crosslinking is established at the beginning of phase (ii); then the observed sagging leads to fits with a decreasing Young modulus Y_{2D} and should, therefore, be discarded as unphysical.

The second, untypical example are H₂O-droplets coated with coagulated films of Ce(SO₄)₂ and CTAB-surfactants, which only show little sagging during crosslinking and even develop wrinkles already during phase (ii), which is a strong hint that a solid membrane had been established early in phase (ii). The crosslinking process is much slower for these capsules. Here, fits with the Laplace-Young shape equations give a decreasing γ that reaches a plateau; the resulting fit errors are, however, quite large and growing in time. The assumption that the shape in the beginning of phase (ii) is already crosslinked and can be regarded as the elastically relaxed reference shape gives a Young modulus Y_{2D} , which increases sharply in the beginning of phase

(ii) and then reaches a plateau; there is no pronounced decrease in Y_{2D} . Fit errors for this scenario are decreasing in time. The fit errors for the two fitting approaches actually show an intersection point early in phase (ii). Between the beginning of phase (ii) and the intersection point, the capsule shape is adequately described by the liquid model. Beyond the intersection point the elastic model provides a more accurate description than the liquid model. One might conclude that the formation of the network at the interface is completed, when the system passes the intersection point. The surface Young modulus does not change significantly after passing the intersection point, which confirms our conclusion. Comparing fit errors could serve as a simple method to estimate the time needed to build a crosslinked solid shell for different materials or chemical processes.

6. Software overview

The software and source code [39] provided with this paper are freely available at github.com under a GPL license [35]. It is a command line program developed in C/C++ and most compatible with Linux/Unix. Usage is fairly simple and a guideline (README.md) is provided as part of the github repository. We give a brief description of how the program works and how the typical workflow looks like.

Presuming that at least one image of the reference capsule and at least one image of a deformed capsule is given, a first call `OpenCapsule` will establish the workspace, i.e., create folders for the input/output files as well as a standard configuration file. The essential information in the configuration file should be updated according to the needs. In particular, the density difference $\Delta\rho$ between the inner and the outer phase is needed, as well as the outer capillary diameter b . Both can be manipulated via the corresponding environment variables `EXPERIMENT_DENSITY` and `EXPERIMENT_CAPDIAMETER`. In addition, the names and paths of the image files need to be specified. Files have to be listed (separated by colons) next to the environment variables `REFERENCE_SHAPE` and `ELASTIC_SHAPE`. Note that the software searches for images by default in the `./input/`-folder. If images are placed somewhere else, the path should be specified via the variable `INPUT_FOLDER`. Requirements for capsule images are detailed in the appendix.

This suffices to run the first analysis. To check if everything works correctly the command `OpenCapsule -r` should be called, which will analyze the reference shapes and determine the surface tension as an average

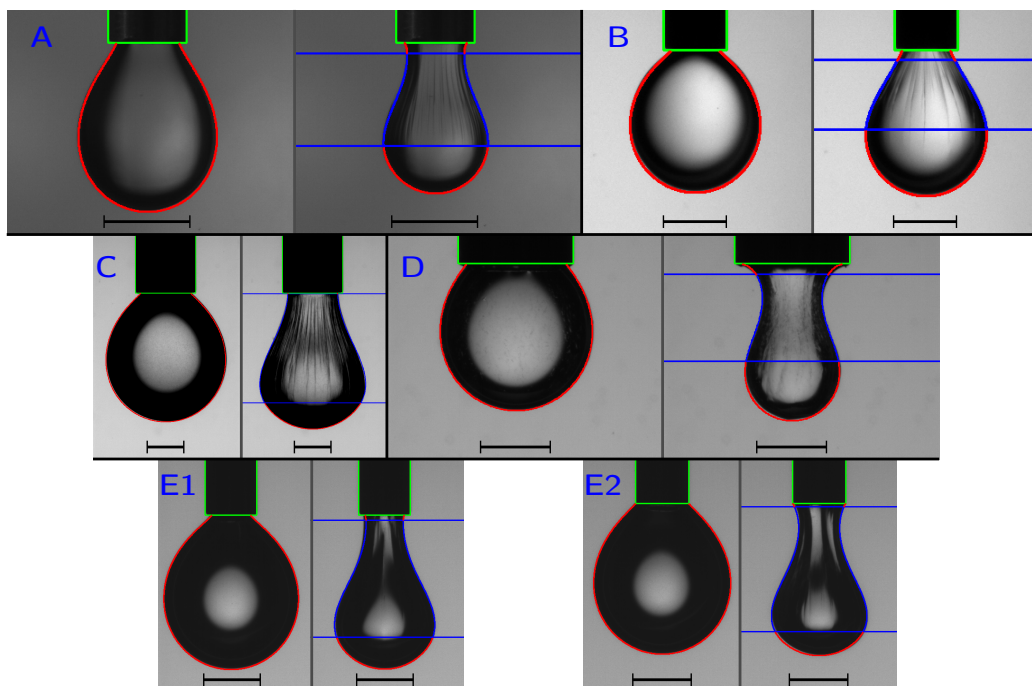


Figure 4: Pendant capsule elastometry results for five different types of capsules. The above images are the original input files overlaid with the best fit theoretical contour, the scale-bar is of length 1 mm. These images are automatically generated by our Software. **A)** Reference and deflated shape of a FC-40 droplet coated with supramolecular polymers and crosslinked with cucurbit[8]uril in H₂O [18]. Both the capsule contour and the wrinkling region are perfectly described by the elastic model. The Laplace-Young analysis yields a surface tension $\gamma = 20.0$ mN/m. The elastic analysis yields an area compression modulus $K_{2D} = 44$ mN/m, a Poisson ratio $\nu_{2D} = 0.29$, a bending modulus $E_B = 5 \cdot 10^{-16}$ Nm and a layer thickness $H = 256$ nm. **B)** Reference and deflated shape of a dodecane droplet coated with three layers of PMAA/PVP in H₂O [38]. The Laplace-Young analysis yields a surface tension $\gamma = 13.2$ mN/m. The elastic analysis yields an area compression modulus $K_{2D} = 141$ mN/m, a Poisson ratio $\nu_{2D} = 0.75$, a bending modulus $E_B = 2.20 \cdot 10^{-14}$ Nm and a layer thickness $H = 1.28$ μ m. **C)** Reference and deflated shape of an OTS-capsule, i.e., *p*-xylyl droplet in solution with 1,2,4-trichlorobenzene and coated with OTS in a glycerol-water mixture, see also Fig. 7, **D)** Reference and deflated shape of a Span 65 capsule, i.e., H₂O-droplet coated with Span 65 (sorbitan tristearate) in dodecane, see also Fig. 6 (left). **E)** Reference and deflated shape of an amino-functionalized polyacrylamide capsule, i.e., H₂O-droplet with Na₂CO₃, N-(3-Aminopropyl)-methacrylamide, and DTAB **E1)** or CTAB **E2)** surfactants, surrounded by an outer phase with *p*-xylyl and sebacoyl dichloride, see also Fig. 6 (right). For all five capsule types predicted wrinkle regions (blue lines) fit the actual wrinkled area quite well. The wrinkles of the Span 65 capsule are hardly visible by eye, probably because of a very thin shell and, thus, a small wrinkle wavelength. Span 65 is expected to form molecular monolayers, which is consistent with this interpretation.

over all given images and, of course, for each individual image. This analysis can also be used to fit the deformed shapes with the Laplace-Young equation, e.g. to determine the Gibbs-modulus. If the results are satisfactory, the command `OpenCapsule -s` will run the elastic analysis. Both types of analyses are completely automatized. The essential numerical results are placed in the `./global_out/`-folder. The results for the reference shapes are listed in `reference.dat`; the results for the deformed shapes in `sequence.dat`. Though no graphical user interface is provided, the results will be printed in a comprehensive html-report, which can be opened in a web browser. This report contains the orig-

inal capsule images with an overlay of the theoretical shape and a scale bar (see Fig. 4), from which one can instantly judge if the fitting procedure was successful. In case of failure, one should adapt the configuration file according to the guideline. Setting up a proper configuration file once for a specific capsule type is typically sufficient. Afterwards it can be used without changes for the same type of capsules.

7. Reference analysis

The shape analysis is split into two batched parts, which are (i) reference shape analysis and (ii) deformed

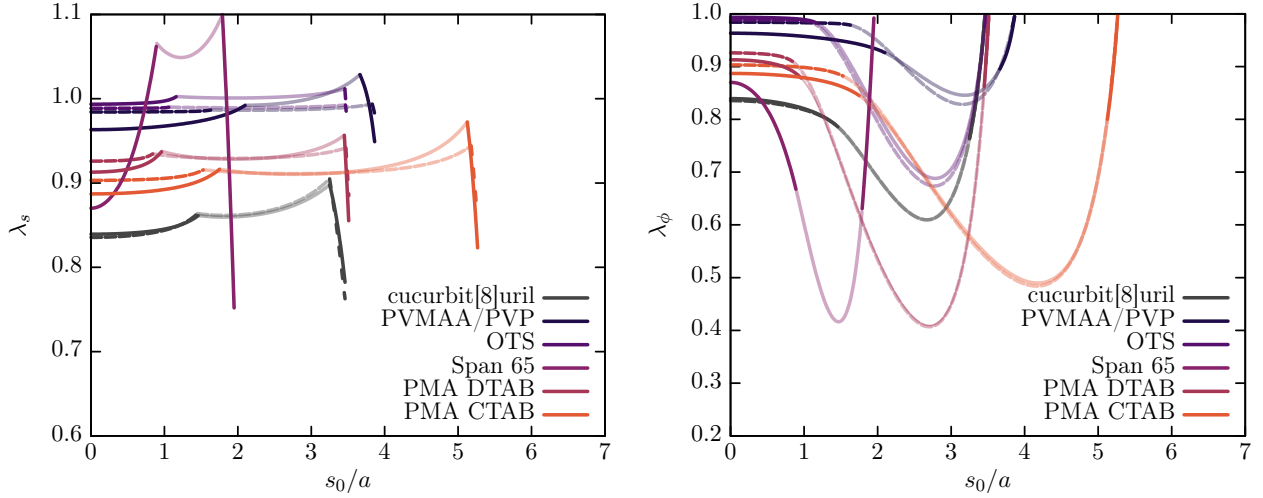


Figure 5: Stretching factors $\lambda_{s,\phi}$ along the deflated capsule contours from Fig. 4 obtained from shape regressions with the nonlinear Hookean elasticity (solid lines), and the Mooney-Rivlin or neo-Hookean elasticity model (dashed lines). The wrinkled region is indicated by transparent lines (either solid or dashed) for both elasticity models. **Left:** Meridional stretching factor λ_s as a function of the arc length s_0 . Except of the cucurbit[8]uril and the Span 65 capsules, all capsules have small strains $|\lambda_s - 1| < 0.1$ and, thus, can be successfully treated with small strain approximations, i.e., the nonlinear Hookean elasticity model. **Right:** Circumferential stretching factor λ_ϕ (apparent stretch $\bar{\lambda}_\phi$ in the wrinkled region) as a function of s_0 . Particularly in the wrinkled region, we see significant deviations from the small strain limit $|\lambda_\phi - 1| < 0.1$. In the wrinkled region we use, however, a different constitutive law ($\tau_\phi = 0$) independent of $\bar{\lambda}_\phi$. In the non-wrinkled region, we find again small strains $|\lambda_\phi - 1| < 0.1$ for PVMAA/PVP, OTS, and polyacrylamide capsules.

shape analysis. For the former one it is advantageous to analyze as many images as possible showing the same, undeformed state of the capsule. This is particularly necessary if images are slightly blurred from camera shake or capsule motion. Averaging over all images improves accuracy, which is important here, since we use the reference shape and parameters during the complete analysis of the deformed shapes. The reference analysis gives the surface tension γ and the shape profile that is necessary to define the strains in the elastic analysis.

From the experiment we know the outer capillary diameter b and the density difference $\Delta\rho$ both in SI units. Solutions of the shape equations have to match the inner capillary of width a , which is the relevant length scale. This quantity is typically specified by the needle manufacturer, but due to material sediments, which potentially change the effective inner capillary diameter, we prefer to measure it directly from the image. Actually, we determine α in units of the image (pixels) by choosing it as an independent fit parameter that rescales all lengths occurring in the Laplace-Young shape equations. From image processing we also know the outer capillary diameter β in units of the image (pixels). Thus, we find $a = \langle \alpha/\beta \rangle b$, which is the effective inner capillary diameter in SI units. Scaling dimensionless lengths with a transforms them to SI units. We introduce dimensionless quantities $\tilde{p}_0 = ap_0/\gamma$ and $\Delta\tilde{\rho} = a^2\Delta\rho g/\gamma$ and mini-

mize the mean square deviation between shape and contour with respect to the parameter set $\mathbf{x}_0 = (\tilde{p}_0, \Delta\tilde{\rho}, \alpha)$. After successful minimization, we obtain the surface tension via $\gamma = a\Delta\rho g/\Delta\tilde{\rho}$. To prepare all contours for the elastic analysis we scale them with $1/\alpha$ and thereby transfer them to dimensionless units.

8. Elastic analysis

In the elastic regression we determine the area compression modulus K_{2D} and the Poisson ratio ν_{2D} by minimizing the mean-square deviations between image contour points and theoretical contour, i.e., with respect to the parameter set $\mathbf{x} = (\tilde{p}, \nu_{2D}, \tilde{K}_{2D})$, where $\tilde{p} = ap/\gamma$ and $\tilde{K}_{2D} = K_{2D}/\gamma$. From these quantities we also obtain the surface Young modulus $Y_{2D} = 2K_{2D}(1 - \nu_{2D})$, see eq. (4). For the Mooney-Rivlin elasticity model we determine analogously the parameter set $\mathbf{x} = (\tilde{p}, \Psi, Y_M)$ within the shape regression. For the neo-Hookean elasticity model we keep $\Psi = 1$ fixed during the shape regression.

It is not required that elastic shapes are ordered chronologically, but it decreases the runtime significantly, since the final parameters of a deformed shape can be used as an initial guess for the following shape, which is probably deformed by a similar extent.

In the current implementation, the pressure p is an additional fit parameter and will also be determined from fitting calculated shapes to an image. In this implementation the elastometry method also serves as pressure measurement and no additional pressure measurement is necessary. If such information is experimentally available from additional measurements, it could be used to improve the results for the elastic moduli, by fixing the pressure to the experimentally obtained value.

After a successful regression we can estimate the bending modulus [19]

$$E_B = \Lambda^4 \bar{\tau}_s / 16\pi^2 L_w^2 \quad (14)$$

by an image analysis of the wrinkles. We determine the length L_w of the wrinkles in meridional direction directly from the shape by finding the zero crossings s_1 and s_2 of $\tau_\phi(s_0)$. The interval $[s_1, s_2]$ in which wrinkles occur sets the meridional extent of the wrinkled region, in which we determine the average meridional tension $\bar{\tau}_s$. It is important to note that the extent of the wrinkled region is not a fit parameter but is predicted by the shape equations and the wrinkling criterion $\tau_\phi < 0$, according to Sec. 4.5. In order to estimate the wrinkling wavelength Λ , we select the wrinkling region from the image and perform an edge detection with high sensitivity and only in horizontal direction to estimate the average distance between the wrinkles, which should correspond to one wavelength Λ . We then count the detected edge pixels N_E and the total number N of pixels in the selected region. The ratio N/N_E now approximately gives the number of wrinkles apparent in the image, if we consider the region as rectangular with equidistant vertical wrinkles. Finally, we use the estimate $\Lambda \approx \pi \bar{r} N_E / N$, where \bar{r} is the capsule radius $r(s_0)$ averaged over the interval $[s_1, s_2]$.

Knowing Y_{2D} , ν_{2D} and E_B , we can directly determine the Föppl von Kármán number $\gamma_{FvK} = Y_{2D} R_0^2 / E_B$ of the capsule, where R_0 is the maximum capsule radius. If we assume that the shell material is a thin layer of a three-dimensional isotropic elastic material, we additionally find the thickness $H = [12E_B(1 - \nu_{2D}^2) / Y_{2D}]^{1/2}$ of the layer, where we use $Y_{2D} = Y_{3D}H$, $E_B = Y_{3D}H^3 / 12(1 - \nu_{3D}^2)$ and $\nu_{3D} = \nu_{2D}$.

9. Applications

In this section we demonstrate the wide applicability of our pendant capsule elastometry software to different capsule materials, see Fig. 4. We apply our software to crosslinked polymeric capsule shell materials like OTS (octadecyltrichlorosilane) (Fig. 4 C) and amino

functionalized polyacrylamide (Fig. 4 E), as well as more exotic capsule materials like Span 65 [40, 41, 42], which is a food emulsifier (Fig. 4 D). Moreover, Fig. 4 shows analyses of two sorts of capsules from literature, cucurbit[8]uril-capsules that have been introduced and discussed in Ref. [18] (Fig. 4 A) and PMAA/PVP-capsules from Ref. [38] (Fig. 4 B). In addition, the method has been used previously (in a less advanced implementation) on hydrophobin-coated air bubbles [19].

As can be seen in Fig. 4, nonlinear Hookean fits for all capsule materials work well and correctly predict the extents of the wrinkled regions (blue lines). The different capsule materials that could be analyzed have quite diverse area compression moduli ranging from $K_{2D} \sim 50$ mN/m (polyacrylamide capsules and cucurbit[8]uril-crosslinked capsules) to $K_{2D} \sim 4$ N/m (OTS-capsules), which corresponds to two orders of magnitude. The bending moduli from the wrinkle analysis range from $E_B = 5 \cdot 10^{-16}$ Nm (cucurbit[8]uril-crosslinked capsules) to $E_B = 10^{-13}$ Nm (OTS-capsules from Fig. 8). For the Span 65 capsules we find even lower bending moduli of order $E_B = 10^{-20}$ Nm assuming a quite short wrinkle wavelengths just below the image resolution. However, the existence of these wrinkles could not be verified experimentally, yet.

Capsules in Fig. 4 develop a “neck” upon deflation. We note that this neck is not associated with any mechanical instability (e.g., a buckling-type instability [37, 43]), i.e., there is no bifurcation between different types of shapes upon deflation but all shapes continuously evolve into the necked shapes. The deflated shapes exhibit high compressional stretches in particular in the wrinkled region as Fig. 5 shows, where the resulting stretches λ_s and λ_ϕ are plotted along the deflated contours for all capsules shown in Fig. 4 and, indeed, values significantly smaller than 1 occur for λ_ϕ . This raises the question whether nonlinear effects are adequately treated by the nonlinear Hookean material model. This model contains nonlinearities only via the $1/\lambda$ -factors in the constitutive relations (3), which arise because we use Cauchy stresses defined per deformed unit length in the force-equilibria.

Our model explicitly includes, however, wrinkle formation, which is a nonlinear phenomenon. We actually use a different constitutive relation $\tau_\phi = 0$ (see eqs. (8) above) in the wrinkled region, such that a further decrease in the apparent stretch $\bar{\lambda}_\phi = \bar{r}/r_0$ in the wrinkled region does no longer lead to increased compressive stresses τ_ϕ but only modifies the effective constitutive law (10) for the meridional stresses $\bar{\tau}_s$ of the pseudo-surface. Therefore, small values of $\bar{\lambda}_\phi$ in the wrinkled region do *not* imply that a different, more appropriate

nonlinear constitutive relation should be used. The results in Fig. 5 show that strains $|\lambda_\phi - 1|$ become large only in this wrinkled region. This suggests that usage of the nonlinear Hookean elasticity is justified.

In order to investigate nonlinear effects further, we also performed fits of all capsules from Fig. 4 with a nonlinear Mooney-Rivlin or neo-Hookean elasticity model. The resulting best fits for the theoretical contour are not distinguishable from the nonlinear Hookean contours shown in Fig. 4, which already suggests that nonlinearities are already adequately treated by the nonlinear Hooke law. In Fig. 5 we also compare the stretches resulting from shape regressions with the nonlinear Hookean and the Mooney-Rivlin or neo-Hookean elasticity model for all deflated capsule shapes from Fig. 4. We see that strains are similar for both models for any of the capsule materials, except of the Span 65 capsules, where we were not able to obtain a reliable fit result using the Mooney-Rivlin elasticity model. For Span 65 the meridional stretching factor varies strongly with the arc length indicating strongly inhomogeneous stresses, which might be the reason for these problems. Treating the dimensionless shape parameter Ψ within Mooney-Rivlin elasticity as an independent fit variable results in $\Psi \rightarrow 1$ for PVMAA/PVP, OTS, polyacrylamide CTAB, and polyacrylamide DTAB capsules. It is noticeable that all these materials give a Poisson ratio $\nu_{2D} > 0.5$ employing the nonlinear Hookean fit. Only for the cucurbit[8]uril capsules, which have a Poisson ratio $\nu_{2D} < 0.5$ we find $\Psi < 1$ and, thus, deviations from the neo-Hookean behavior. This indicates that most of the capsule materials discussed in this paper behave like a neo-Hookean material and, thus, also similar to a nonlinear Hookean material in the small strain limit. This limit is obviously applicable to PVMAA/PVP, OTS and polyacrylamide capsules, since they all satisfy $|\lambda_s - 1| < 0.1$ over the whole contour, and also $|\lambda_\phi - 1| < 0.1$ in the non-wrinkled region. Because of these results and the fact that Mooney-Rivlin fits require a much higher computational cost, we focus on nonlinear Hookean elasticity in the following, which gives good results for all capsule types.

Where comparison to other rheological measurements is possible, results from pendant droplet elastometry are in good agreement. For PVMAA/PVP-capsules, the surface Young modulus of $Y_{2D} = 211 \text{ mN/m}$ agrees with the findings in Ref. [38]. In the following we will discuss results on the OTS-, amino-functionalized polyacrylamide, and Span 65 capsules, which have not been previously discussed in the literature, in more detail. Pendant capsule elastometry allows us to obtain elastic moduli of the two-dimensional capsule shell material

for each digitized image of the deflated capsule shape (given at least one image of its undeformed reference shape). Therefore elastic moduli can be determined as a function of the deflation volume. If the volume change rate can be controlled, elastic moduli can be determined as a function of the volume change rate to investigate viscoelastic effects. If series of images over one or several deflation cycles are available, we can investigate aging effects, for example, by plastic deformation over many deflation cycles. We will explore these possibilities for OTS-, polyacrylamide, and Span 65 capsules, starting with the latter.

9.1. Span 65 capsules

Span 65 has a polar head group connected to three carbon chains leading to intermolecular interactions when adsorbed to a liquid interface. Though not explicitly crosslinked, the material shows elastic properties due to the formation of temporary networks. For Span 65, our method agrees with four different rheological measurements (surface shear-rheometry, Langmuir-Blodgett, spinning-drop method, and shear flow rheoscope), which all give area compression moduli K_{2D} between 0.3 and 0.9 N/m. These fit well to the values $K_{2D} = 0.2 \dots 1.0 \text{ N/m}$ obtained by our method for small deformations at $V/V_0 > 0.8$, see Fig. 6 (left). The pendant capsule elastometry results in Fig. 6 (left) also reveal that the area compression modulus strongly varies with the volume: deflated capsules with $V/V_0 < 0.5$ become very soft with $K_{2D} < 0.1 \text{ N/m}$. This pronounced compression softening can eventually explain the deviations among previous rheological measurements. Upon re-inflating the capsule, the compression modulus exhibits a non-monotonous behavior (see Fig. 6 inset) but we do not find a generic pathway among the eight individual capsules that we analyzed. We can, however, speculate based on visual impressions from the images that the capsule material develops overlaps or similar microscopic folds that vanish after complete re-inflation. As a consequence, we see hysteresis but no aging effects as the compression modulus returns to its original value after completing a deformation cycle, see Fig. 6 (left). We also do not see a pronounced change of this behavior if the volume change rate is changed. All these results suggest that the compression softening could be a result of reversible rearrangements of the temporary network of the capsule material on time scales, which are short compared to the time scale of volume changes. These reversible rearrangements lead to an apparent decrease of elastic moduli with decreasing volume. In Fig. 5 we showed that Span 65 capsules exhibit strongly inhomogeneous strains, which likewise

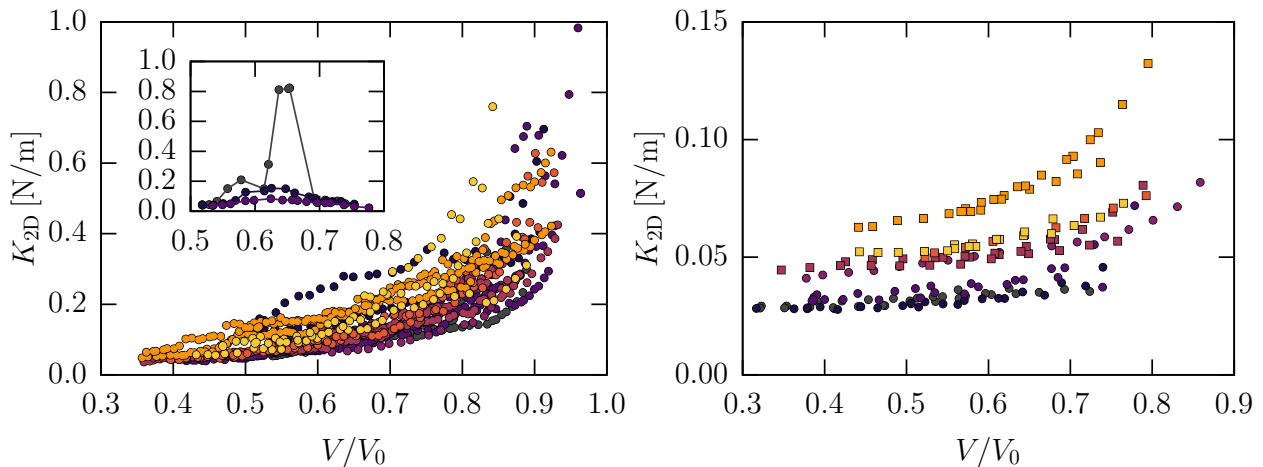


Figure 6: **Left:** Pendant capsule elastometry results for Span 65 capsules, i.e., H_2O -droplets coated with Span 65 (sorbitan tristearate) in dodecane. We analyzed eight individual capsules (color code), most of them fitted over three phases of deflation. The inset also shows the three inflation phases for one of these capsules. The inflation phases differ significantly among the capsules, and there is no generic behavior as for the deflation phases. Among the individual capsules, volume change rates vary between 0.5 and $1.0 \mu\text{l/s}$. Surface shear-rheometry measurements give $K_{2\text{D}} = 0.9 \text{N/m}$, Langmuir-Blodgett trough $K_{2\text{D}} = 0.33 \text{N/m}$, spinning-drop $K_{2\text{D}} = 0.36 \text{N/m}$, and rheoscope $K_{2\text{D}} = 0.54 \text{N/m}$. Rheological measurements are thus consistent with our method, which also reveals a strong variation of $K_{2\text{D}}$ with the volume. The Poisson ratio is roughly given by $\nu_{2\text{D}} = 0.8$. **Right:** Pendant capsule elastometry results for polyacrylamide capsules, i.e., H_2O -droplet with Na_2CO_3 , N -(3-Aminopropyl)-methacrylamide and DTAB (circles) or CTAB (quads) surfactants. The outer phase consists of p -xylyl and sebacoyl dichloride. We analyzed four individual CTAB and four individual DTAB capsules, most of them fitted over three phases of deflation. Deformations were applied after 60 minutes equilibration time with the crosslinker. The Poisson ratio is $\nu_{2\text{D}} = 0.6$ with DTAB surfactants and $\nu_{2\text{D}} = 0.5$ with CTAB surfactants. The values of the area compression modulus are consistent with shear-rheometer measurements, which give $K_{2\text{D}} = 30 \dots 100 \text{mN/m}$.

indicates a quite complex elastic behavior. Eventually, one might conclude that Span 65 is not well described by classical elastic models. Specific models that account for the microscopic details of the material have to be developed to analyze the elastic properties of Span 65 in more detail. In contrast to permanently crosslinked polymer membranes Span 65 forms temporarily crosslinked network structures [44]. Within these structures, the applied stresses can relax with time constants of the order of several minutes, which leads to time-dependent transitions from solid into liquid like membranes. This more complicated rheological behavior, can only be described by time-dependent nonlinear constitutive laws. Bending moduli can not be determined directly from the images since the wrinkles are not visible by eye although the shape analysis suggests the existence of wrinkles over an extended region, see Fig. 4 D. One could assume a wrinkle wavelength just below the image resolution, which gives $\Lambda \leq 8 \mu\text{m}$, $E_B \leq 2 \cdot 10^{-20} \text{Nm}$, and $H \leq 1.67 \text{nm}$. Eventually wrinkles could also be absent in this system because compressive hoop stresses can be relaxed by the rearrangements in the temporary network.

9.2. OTS-capsules

For the OTS-capsules from Fig. 7 we find values $K_{2\text{D}} = 1.0 \dots 4.0 \text{N/m}$, which is just slightly below the rheological data from other methods giving $K_{2\text{D}} = 3.0 \dots 10.0 \text{N/m}$ (spinning drop measurements give $K_{2\text{D}} = 3.0 \dots 7.5 \text{N/m}$ and rheoscope measurements $K_{2\text{D}} = 4.0 \dots 10 \text{N/m}$), see Fig. 7. In Fig. 7, we analyzed a single OTS-capsule for different volume change rates ranging from 0.5 (slow) to $10.0 \mu\text{l/s}$ (fast). In principle, this enables us to see viscoelastic effects. We expect a viscoelastic material to exhibit a smaller shear modulus μ' for slow deformation such that creep or viscoelastic relaxation is possible. Fig. 7 shows that the surface Young modulus and the shear modulus $\mu' = K_{2\text{D}}(1 - \nu_{2\text{D}})/(1 + \nu_{2\text{D}})$ are both significantly decreased for *higher* volume change rates. Therefore, this is probably an effect of aging rather than viscoelastic behavior. It is thereby difficult to explain the increased area compression modulus and Poisson's ratio, which indicates that the capsule material tends to become incompressible due to microscopic effects, that cannot be observed in detail experimentally. However, by exploring volume cycles for a wide range of volume change rates, it should, in principle, be possible to determine the frequency dependence of the surface shear (storage) modulus μ' from these measurements. Therefore, in-

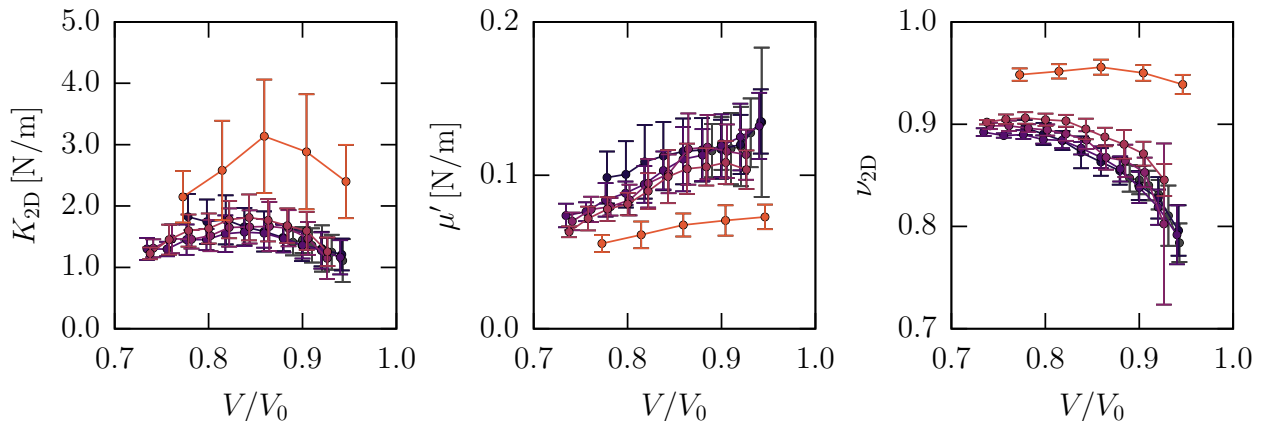


Figure 7: Pendant capsule elastometry results for OTS-capsules, i.e., a *p*-xylol droplet in solution with 1,2,4-trichlorobenzene and coated with OTS in a glycerol-water mixture. We analyzed a single individual capsule with a volume change rate of $0.5 \mu\text{l/s}$ (points) and total volume reductions of $2.5 \mu\text{l}$ (gray), $5.0 \mu\text{l}$ (blue), $7.5 \mu\text{l}$ (dark violet), $10.0 \mu\text{l}$ (light violet), $12.5 \mu\text{l}$ (red). The same capsule was analyzed with step-wise increased volume change rates (1.0, 2.5, 5.0, $7.5 \mu\text{l/s}$) up to $10 \mu\text{l/s}$ (orange) and the same total volume reductions. The capsule was subject to 30 cycles of de- and inflation, and we analyzed 1674 images for the first and last five cycles, which allows us to calculate error bars by averaging over small volume ranges. Spinning drop measurements give $K_{2D} = 3.0 \dots 7.5 \text{ N/m}$ and rheoscope measurements $K_{2D} = 4.0 \dots 10 \text{ N/m}$, depending on which Poisson ratio ν_{2D} is assumed to obtain K_{2D} from the actually measured Y_{2D} . These values are slightly higher than our pendant elastometry measurements. For the Poisson ratio we get roughly $\nu_{2D} = 0.85$, which is slightly above previous measurements predicting $\nu_{2D} = 0.5 \dots 0.8$ [29]. We see that, for the last 5 cycles with a volume change rate of $10.0 \mu\text{l/s}$ (orange), the material has softened significantly, regarding Y_{2D} and μ' . The area compression modulus K_{2D} increased, however, due to an increased Poisson ratio. In principle, these effects could either be induced by aging or by viscoelastic effects. For viscoelastic materials we typically expect a stiffening when volume change rates are increased. Therefore, we suggest that this softening is induced by aging at the intermediate rates 1.0, 2.5, 5.0 and $7.5 \mu\text{l/s}$ 54 that have been applied before the final $10.0 \mu\text{l/s}$ rate.

dividual capsules should be prepared for each volume change rate to eliminate the influence of aging.

For OTS-capsules (with different liquid phases compared to those in Fig. 7) we analyzed aging effects in more detail in Fig. 8 by monitoring the change of elastic constants over three consecutive deformation cycles of the same capsule. For this capsule, the deformation behavior becomes approximately reversible only after completing two deflation-inflation cycles. The first two cycles exhibit hysteresis hinting to plastic deformation in the capsule. Similar effects can be seen in Fig. 7, where the OTS-capsule was subject to 30 de- and inflation cycles in total. The orange circles show the last five cycles where we observe a softening regarding the shear modulus, a stiffening regarding the area compression modulus, as well as an increased Poisson ratio. For all quantities the volume dependence is weakened. Capsules from Fig. 7 obviously exhibit a more complex aging behavior, which can only be caused by the different liquid phases (essentially oil and water phase swapped), because the OTS shell material is the same. However, these results suggests that by iteratively applying small volume change rates and small total volume reductions, capsule deformations can reach a reversible regime, where subsequent deformation cycles yield the same elastic constants and aging is effectively absent.

If, however, the volume change rates or total volume reductions are successively increased, aging proceeds and the capsule material becomes even softer.

By applying the wrinkling analysis to the capsules from Fig. 7 we measure wrinkling wavelengths $\Lambda = 0.2 \text{ mm}$ leading to a bending modulus of $E_B = 10^{-15} \dots 10^{-14} \text{ Nm}$ and a thickness $H = 90 \dots 290 \text{ nm}$. Electron microscopy measurements give $H = 100 \dots 1000 \text{ nm}$, which roughly agrees. The quality of these estimates depends crucially on the measurement of the wrinkling wavelength since we have $E_B \propto \Lambda^4$. We prefer to measure Λ at the bottom of the wrinkles, because length measurements in the center of the capsule can be better translated to the length scale prescribed by the outer capillary diameter.

9.3. Polyacrylamide capsules

We tested our software also on amino functionalized polyacrylamide capsules formed with two different surfactants CTAB and DTAB, see Fig. 6 (right). For the CTAB polyacrylamide capsules we find area compression moduli in the range $K_{2D} = 50 \dots 100 \text{ mN/m}$ and a Poisson ratio $\nu_{2D} = 0.5$, for the DTAB polyacrylamide capsules we find $K_{2D} = 30 \dots 60 \text{ mN/m}$ and $\nu_{2D} = 0.6$. These values are consistent with surface shear-rheometry measurements giving $K_{2D} =$

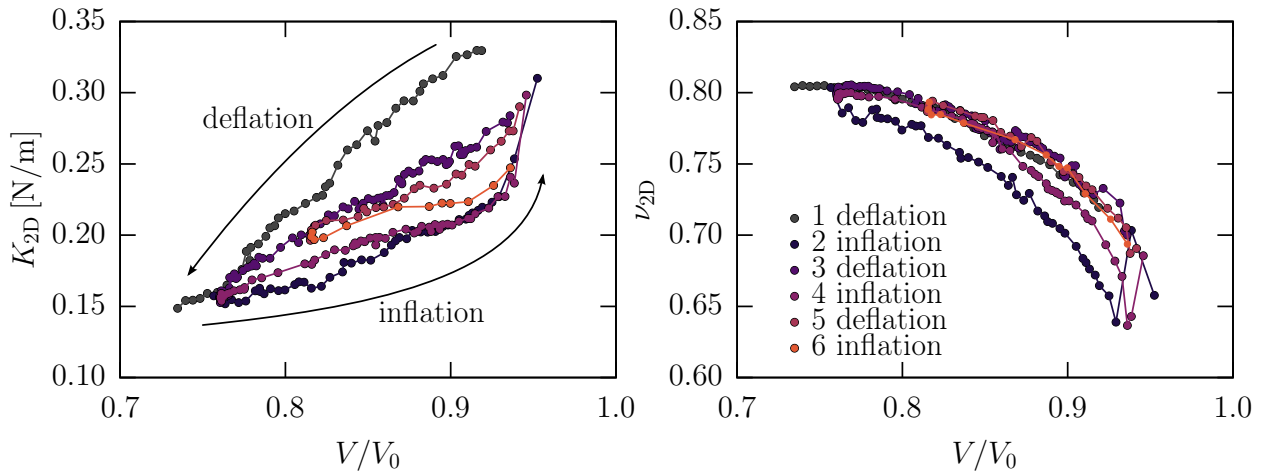


Figure 8: We analyze a single OTS-capsule [19], i.e., a H_2O -droplet coated with OTS in *p*-xytol, for three consecutive deflation and inflation cycles. This reveals aging effects: deformations become nearly reversible after two complete deformation cycles. For the first two cycles we clearly see hysteresis. Note that these OTS-capsules exhibit much smaller values of the area compression modulus K_{2D} compared to those in Fig. 7. Since both capsule membranes are made from OTS, and both should have a similar thickness ranging from 100 to 1000 nm, we conclude that this has to originate in the different liquid phases that have been used. Here, a water droplet was used in a *p*-xytol phase, whereas for the capsules in Fig. 7 a *p*-xytol droplet was used in a glycerin-water mixture. This possibly influences the network forming process, such that capsules from Fig. 7 appear more like an incompressible material.

30...100 mN/m. Our pendant capsule elastometry results show that the elastic properties of this type of capsule can be tuned by changing only the surfactants (CTAB vs. DTAB) and not the crosslinker. Fig. 6 (right) clearly shows that CTAB gives consistently stiffer capsules than DTAB. Bending moduli for the DTAB polyacrylamide capsules are slightly smaller than for the CTAB polyacrylamide capsules. We find $E_B = 10^{-14}$ Nm for CTAB and $E_B = 8 \cdot 10^{-15}$ Nm for DTAB (using images from Fig. 4).

10. Gibbs modulus

Finally, we like to discuss why the Gibbs modulus is not suitable to analyze solid-like elastic shell materials. As mentioned above, the Gibbs modulus $E_{\text{Gibbs}} = d\gamma/d\ln A$ is frequently determined from measurements of an “effective surface tension” γ describing the solid shell interface as a function of the surface area A . We use the term “effective” here, because, in principle, one cannot determine a surface tension from deformations of a solid shell interface. The Gibbs modulus E_{Gibbs} is equal to the area compression modulus K_{2D} for a fluid interface or for a two-dimensional solid interface in a planar Langmuir-Blodgett trough geometry.

It is possible to determine the Gibbs modulus by using a standard pendant drop tensiometer measuring only the surface tension and the surface area. Commercial pendant drop tensiometers apply sine-like vol-

ume changes and determine the complex Gibbs modulus with an elastic and a viscoelastic contribution. This type of analysis is sometimes referred to as the “oscillating drop” method.

To be consistent with our purely elastic model, we apply a linear fit in the $(\ln A, \gamma)$ -plane. For the OTS-capsules we find $E_{\text{Gibbs}} = 40$ mN/m, which is two orders of magnitude below the actually measured area compression moduli. Similar results were obtained in Ref. [19], where E_{Gibbs} and K_{2D} were compared for theoretically generated shapes. For the Span 65 capsules we get $E_{\text{Gibbs}} = 33$ mN/m, which is one order of magnitude below the value obtained in the Langmuir-Blodgett trough. We obtained similar values $E_{\text{Gibbs}} \approx 40$ mN/m by applying the oscillating drop method to Span 65 capsules, which explicitly demonstrates that determining the Gibbs modulus with a pendant drop tensiometer leads to misleading results, as already stated in Ref. [19]. The deformed shapes of elastic capsules cannot be fitted accurately with the Laplace-Young equation for fluid interfaces as we have already shown in Fig. 3. Moreover, the relation between Gibbs modulus and area compression modulus K_{2D} becomes non-trivial and geometry-dependent because of inhomogeneous elastic stresses in the capsule geometry and the existence of a curved undeformed reference shape of the capsule. Only in a planar geometry, where the elastically relaxed reference state is planar and where stresses remain homogeneous, the Gibbs modulus coin-

cides with the area compression modulus.

11. Conclusion

We developed an efficient and completely automated C/C++ software in order to perform pendant capsule elastometry in pendant drop devices. The analysis is based on a thin elastic shell model of the capsule interface and, thus, applies for elastic solid capsule materials. Such materials can be recognized, for example, by their ability to develop wrinkles.

The analysis requires a reference shape, for which we usually assume that it can be described by a liquid Laplace-Young shape if the shell material is crosslinked at a liquid interface. A minimum set of two images, one of the reference shape and another of a deformed shape, and two experimental parameters, namely the density difference $\Delta\rho$ and the outer capillary diameter b , are sufficient to run the complete analysis and obtain values for Young's modulus and Poisson's ratio using the Hookean elasticity model, or, alternatively, the Rivlin modulus and the dimensionless shape parameter using the Mooney-Rivlin elasticity model. In addition, if wrinkling occurs, the bending modulus and, thus, the shell thickness can be determined from a wrinkle wavelength measurement.

More interesting results are often obtained, if a whole sequence of deformed states can be analyzed in chronological order, which makes it possible to investigate the dependence of the elastic moduli on the capsule volume. This is where possible phase transitions, hysteresis and aging effects, or plastic deformations of the material could be detected. Future work should explore whether a frequency-dependent surface shear (storage) modulus μ' can be reliably determined by measurements at different volume change rates.

In our present implementation pendant capsule elastometry does not require experimental information on the pressure p but rather serves itself as a pressure measurement because p is determined by shape fitting. If such pressure is measured independently, this additional information can be readily used to improve the results for the remaining fit parameters by setting p to a constant value within shape regression. This option is supported by the current version of our software. But there are also other possibilities to use the pressure information, e.g., to directly calculate local stresses in the deformed state from additional image information on local curvatures and radii [17]. This additional stress information can then be used to improve the shape fitting procedure beyond simple elimination of one fit parameter [45].

In the present form of the code, we provide linear Hookean elasticity, nonlinear Hookean elasticity, and Mooney-Rivlin or neo-Hookean elasticity to describe the elastic behavior of the shell material. We find that the nonlinear Hookean model gives the best compromise between accuracy and performance. Moreover, we randomly checked the results against Mooney-Rivlin elasticity (which is much slower due to numerical determination of the closure relations). This revealed that both elasticity models give similar results over a wide range of materials and deformation behavior. We find that the simple linear Hookean elasticity can only describe very small deformations compared to nonlinear Hookean or Mooney-Rivlin elasticity. We gained this insight from generating theoretical shapes, where we decreased the pressure successively, thereby simulating proceeding deflation. Numerics for the linear Hookean elasticity failed much earlier in fulfilling the required boundary conditions, which is necessary to generate a valid shape. It remains to be verified systematically, however, what differences eventually arise between fitting with different elasticity models. Fitting with the most appropriate model should produce the least elastic parameter variation as a function of the volume.

For certain materials the use of even more specific elastic models is more appropriate, for example, hydrophobins coating air bubbles [6, 19] act as interfacial rafts of hard particles with soft shells, which require a more refined elastic description to interpret capsule shapes correctly and avoid jumps in elastic constant in elastometry fits [46]. Therefore, future work should also aim at implementing different elastic models in order to compare fit results for different models and determine the most appropriate model from the data. In particular, for the Span 65 investigated in this paper, we suggest to develop such microscopic models, because we found strongly inhomogeneous strains and generally atypical elastic behavior. Moreover fit results revealed a pronounced compression softening, which we did not find for any other capsule material, which also hints to the use of a more appropriate elasticity model.

As we have shown, our software for pendant drop devices is widely applicable. We tested it on different materials and the results are in good agreement with available rheological data. We make the OpenCapsule software freely available under the GPL license [35] at github.com/jhegemann/opencapsule. A user manual is also available as Supplementary material.

12. Acknowledgements

We thank Sandrine Le Tirilly and Cécile Monteux for providing capsule images from capsules used in Ref. [38] (Fig. 4 B) and Andrew Salmon and Chris Abell for providing images from capsules used in Ref. [18] (Fig. 4 A). Moreover we thank Patrick Degen for providing the capsule images analyzed in Figs. 8. We thank Horst-Holger Boltz and Tobias Kampmann for a careful reading of the manuscript and fruitful discussions.

Appendix A. Least squares

Both the shooting method and the shape regression require least square error/deviation minimization. Fitting shape equations to experimental contours is implemented by a nested minimization algorithm, which minimizes the distance between individual shape segments (and the boundary conditions) in an inner loop, which we call *shooting method* (see Sec. Appendix C below), and the deviation between theoretical shape and contour in an outer loop, which we call *shape regression* (see Sec. Appendix D below). At first, we characterize the error function that has to be minimized within the least square algorithm.

Consider a global residual vector

$$\mathbf{F}(\mathbf{x}) = (\varphi_1(\mathbf{x}), \dots, \varphi_N(\mathbf{x}))^T \quad (\text{A.1})$$

assembling the individual residuals φ_i that depend on an arbitrary parameter set \mathbf{x} . In case of the shooting method, the residuals φ_i are defined by the distances between consecutive shape segments and, finally, between the last shape segment and the boundary condition. Thus, the parameter set \mathbf{x} can be identified with the set of shooting parameters, which are the initial values of the individual shape segments. In case of the shape regression, the residuals φ_i give the shortest distances between the discrete points of the contour (obtained from the image) and the theoretical shape profile given by a solution of the shape equations. Thus, the parameter set \mathbf{x} can be identified with the shape parameters characterizing the solutions of either the Laplace-Young equations (1) or the elastic shape equations (2).

We now introduce the general least square method, stressing again that we use this method for both the shooting method *and* the shape regression. The Jacobian \mathbf{J}_F measures the change of $\mathbf{F}(\mathbf{x})$ at some point \mathbf{x} . In order to minimize the euclidean norm $\|\mathbf{F}(\mathbf{x})\|$ with respect to \mathbf{x} we linearize $\mathbf{F}(\mathbf{x})$ within a small region $\Delta\mathbf{x}$ according to

$$\|\mathbf{F}(\mathbf{x} + \Delta\mathbf{x})\| \approx \|\mathbf{F}(\mathbf{x}) + \mathbf{J}_F \Delta\mathbf{x}\| \stackrel{!}{=} 0 \quad (\text{A.2})$$

yielding the linear and typically over-determined system of equations

$$\mathbf{J}_F \Delta\mathbf{x} = -\mathbf{F}(\mathbf{x}). \quad (\text{A.3})$$

Standard algorithms like the Gauss-Newton method solve the quadratic normal equation

$$\mathbf{J}_F^T \mathbf{J}_F \Delta\mathbf{x} = -\mathbf{J}_F^T \mathbf{F}(\mathbf{x}), \quad (\text{A.4})$$

but we prefer to directly solve (A.3), because the condition of $\mathbf{J}_F^T \mathbf{J}_F$ can be poor in comparison to the condition of \mathbf{J}_F , i.e.,

$$\text{cond}(\mathbf{J}_F^T \mathbf{J}_F) \sim \text{cond}(\mathbf{J}_F)^2. \quad (\text{A.5})$$

We do so by decomposing $\mathbf{J}_F = \mathbf{Q}\mathbf{R}$ via Householder transformations and multiplying with \mathbf{Q}^T ,

$$\mathbf{R}\Delta\mathbf{x} = -\mathbf{Q}^T \mathbf{F}(\mathbf{x}), \quad (\text{A.6})$$

where we used that $\mathbf{Q}^T \mathbf{Q} = \mathbb{1}$. Note that this yields

$$\mathbf{R} = \begin{pmatrix} \mathbf{R}_0 \\ 0 \end{pmatrix} \quad (\text{A.7})$$

and

$$\mathbf{Q}^T \mathbf{F}(\mathbf{x}) = \begin{pmatrix} \mathbf{b}_0 \\ \mathbf{b}_1 \end{pmatrix} \quad (\text{A.8})$$

in case of over-determined systems, such that the solution is given by

$$\Delta\mathbf{x} = \mathbf{R}_0^{-1} \mathbf{b}_0 \quad (\text{A.9})$$

with a finite error

$$\|\mathbf{F}(\mathbf{x}) + \mathbf{J}_F \mathbf{R}_0^{-1} \mathbf{b}_0\| = \|\mathbf{b}_1\|. \quad (\text{A.10})$$

Applying the parameter shift $\Delta\mathbf{x}$ resulting from (A.9) or (A.3) iteratively to the current parameter set finally gives a solution \mathbf{x}^* , which minimizes $\|\mathbf{F}(\mathbf{x})\|$, i.e.,

$$\min_{\mathbf{x}} \|\mathbf{F}(\mathbf{x})\| = \mathbf{x}^*. \quad (\text{A.11})$$

To obtain the sequence $\{\mathbf{x}^k\}$ that finally converges to \mathbf{x}^* , we use the update scheme

$$\mathbf{x}^{k+1} = \mathbf{x}^k + \lambda_j \Delta\mathbf{x}^k, \quad (\text{A.12})$$

where λ_j is chosen such that $\|\mathbf{F}(\mathbf{x})\|$ decreases in each step of iteration. Several line search methods may be applied here, but, in view of efficiency, we prefer to chose $\lambda_j = 1/2^j$, where we increase j starting from $j = 0$ until

$$\|\mathbf{F}(\mathbf{x}^k + \lambda_j \Delta\mathbf{x})\| < \|\mathbf{F}(\mathbf{x}^k)\|. \quad (\text{A.13})$$

This is sometimes referred to as a ‘‘backtracking line search’’ method. The minimization algorithm will be

used for the multiple shooting method, where (A.3) is quadratic, as well as for the final regression of the shape equations, where (A.3) is strongly over-determined. Since we exclusively use numerical differential quotients the algorithm converges linearly, whereas a classical Newton minimization would converge quadratically due to analytical derivatives.

Appendix B. Reference shape

Obtaining a shape profile from the set of shape equations (1) is trivial, since there are no shooting parameters. In practice, one integrates the set of shape equations (1) (while increasing the arc length s_0) until $r_0(s_0) = a/2$ is satisfied for the second time, meaning that the shape enters the capillary from $r_0 > a/2$ (there is also a solution, which enters the capillary for the first time from $r_0 < a/2$; this solution has a much smaller volume and does usually not correspond to the experimental reference shape). The arc length s_0 that satisfies this condition is chosen as the undeformed contour length L_0 , such that $r_0(L_0) = a/2$. Note that the undeformed length L_0 is fixed for the deformed shape profiles. The resulting reference shape

$$\mathbf{y}_0(s_0, \mathbf{x}_0) = \begin{pmatrix} r_0(s_0, \mathbf{x}_0) \\ z_0(s_0, \mathbf{x}_0) \\ \psi_0(s_0, \mathbf{x}_0) \end{pmatrix} \quad (\text{B.1})$$

is obtained as a function of of the parameter set $\mathbf{x}_0 = \{p_0, \rho, a\}$, which are adapted during the shape regression (see Sec. Appendix D) to optimally match the contour points extracted from the image.

Appendix C. Shooting method

Solving the elastic shape equations requires a shooting method to be applied, because of the unknown initial tension $\tau_s(0) = \mu$ at the capsule's apex. For a given initial value μ we therefore integrate the shape equations starting at the capsule's apex from $s_0 = 0$ to $s_0 = L_0$, where L_0 was determined before by satisfying the boundary condition of the Laplace-Young reference shape. We thereby obtain a deformed shape trajectory $\mathbf{y}(s_0; \mu)^T$, which depends on the reference shape via the shape profile $r_0(s_0)$ and the length of the undeformed contour L_0 . However, the deformed length $L = \int_0^{L_0} \lambda_s ds_0$ of course adapts according to the stretch factor λ_s . For a capsule with inner capillary width a centered at $r = 0$ a valid solution has to satisfy the boundary

condition

$$f(\mu) = r(L_0; \mu) - a/2 \stackrel{!}{=} 0. \quad (\text{C.1})$$

The function $f(\mu)$, which is measured from the solution $\mathbf{y}(s_0; \mu)^T$, has to be minimized by applying a bisection with respect to the parameter μ . We recommend a bisection in this case, because the function $f(\mu)$ is very steep, particularly for large area compression moduli K_{2D} . The algorithm is assumed to be converged if $|f(\mu)| < \epsilon_{\text{single}}$. Note that our software takes this as a minimum criterion, i.e., it tries to minimize $|f(\mu)|$ even further until the interval within the bisection method becomes smaller than 10^{-16} . It is generally important to minimize $|f(\mu)|$ as far as possible, because the shape trajectories are very sensitive to the initial value μ .

In cases where the required accuracy ϵ_{single} can not be reached, we further improve solutions by applying a multiple shooting method subsequently. For this purpose we divide the interval $[0, L_0]$ in q sub-intervals with $q + 1$ grid points at $s_k = k L_0/q$, where $k = 0, \dots, q$. On the sub-interval $[s_k, s_{k+1}]$ we define the k -th segment

$$\mathbf{y}_k(s_0) \equiv \mathbf{y}_k^0 + \int_{s_k}^{s_0} ds'_0 \mathbf{f}(\mathbf{y}(s'_0); \mathbf{y}_k^0) \quad (\text{C.2})$$

by integrating the set of shape equations

$$\mathbf{y}' = \mathbf{f}(\mathbf{y}(s_0); \mathbf{y}_k^0), \quad (\text{C.3})$$

starting at

$$\mathbf{y}_k^0 = (r_k^0, z_k^0, \psi_k^0, \tau_k^0) \in \mathbb{R}^4 \quad (\text{C.4})$$

and ending at

$$\mathbf{y}_k \equiv \mathbf{y}_k(s_{k+1}, \mathbf{y}_k^0) \in \mathbb{R}^4. \quad (\text{C.5})$$

Note that the final segment \mathbf{y}_{q-1} has to match the final grid point \mathbf{y}_q . Having decomposed the continuous solution in q individual segments, we track the k -th residual vector separating the k -th and $(k + 1)$ -th segment via

$$\boldsymbol{\varphi}_k = \begin{cases} \mathbf{y}_k - \mathbf{y}_{k+1}^0 \in \mathbb{R}^4 & k = 1 \dots q - 2 \\ \mathbf{y}_{k,1} - \mathbf{y}_{k+1,1}^0 \in \mathbb{R}^1 & k = q - 1. \end{cases} \quad (\text{C.6})$$

The last segment and grid point, $\mathbf{y}_{q-1,1} = r_{q-1}(s_q)$ and $\mathbf{y}_{q,1}^0 = r_q^0 = a/2$, define the final boundary condition (C.1), where the capillary has to be matched. Any other residual corresponds to continuity conditions that ensure a smooth shape. To arrange the segments into a continuous solution while satisfying the boundary condition at the capillary, we have to set up the Jacobians for each segment \mathbf{y}_k , where $k \in [0, q - 1]$, with respect to the corresponding initial values \mathbf{y}_k^0 . At s_0 only τ_0^0 can be chosen freely, whereas $r_0^0 = 0$, $z_0^0 = \zeta$ and $\psi_0^0 = 0$

are fixed due to axis symmetry. At s_q we have to satisfy the boundary condition $r_{q-1}(s_q) - a/2 = 0$ whereas $z_{q-1}(s_q)$, $\psi_{q-1}(s_q)$ and $\tau_{q-1}(s_q)$ are arbitrary. The Jacobian \mathbf{J}_0 corresponding to \mathbf{y}_0 is a column vector in \mathbb{R}^4 , the Jacobian \mathbf{J}_{q-1} corresponding to \mathbf{y}_{q-1} is a row vector in \mathbb{R}^4 . All intermediate Jacobians \mathbf{J}_k with $k = 1, \dots, q-2$ are quadratic matrices in $\mathbb{R}^{4 \times 4}$ and we can write them as

$$\mathbf{J}_0 = \frac{\partial \mathbf{y}_0}{\partial \tau_0^0}, \quad \mathbf{J}_k = \frac{\partial \mathbf{y}_k}{\partial \mathbf{y}_k^0}, \quad \mathbf{J}_{q-1} = \frac{\partial r_{q-1}}{\partial \mathbf{y}_{q-1}^0}, \quad (\text{C.7})$$

where we use differential quotients

$$\frac{\partial \mathbf{y}_k}{\partial \mathbf{y}_{k,i}^0} = \frac{1}{2\Delta} \left(\mathbf{y}(s_{k+1}; s_k, \mathbf{y}_k^0 + \Delta \mathbf{e}_i) - \mathbf{y}(s_{k+1}; s_k, \mathbf{y}_k^0 - \Delta \mathbf{e}_i) \right) \quad (\text{C.8})$$

with canonical unit vectors \mathbf{e}_i and $i = 1, \dots, 4$. Note that we typically use $\Delta = 10^{-6}$. Finally we find the block-matrix

$$\mathbf{J} = \frac{\partial(\mathbf{y}_0 - \mathbf{y}_1^0, \dots, \mathbf{y}_{q-1,1} - \mathbf{y}_{q,1}^0)}{\partial(\mathbf{y}_0^0, \dots, \mathbf{y}_{q-1}^0)} = \begin{pmatrix} \mathbf{J}_0 & -\mathbb{1} & \dots & 0 \\ \vdots & \ddots & \ddots & \vdots \\ \vdots & & \ddots & -\mathbb{1} \\ 0 & \dots & \dots & \mathbf{J}_{q-1} \end{pmatrix}, \quad (\text{C.9})$$

where $\mathbb{1} \in \mathbb{R}^4$ denotes the identity matrix. Applying the least square minimization method described above, i.e., solving the quadratic system $\mathbf{J}_F \Delta \mathbf{x} = -\mathbf{F}$ iteratively, where

$$\mathbf{F} = (\boldsymbol{\varphi}_0, \dots, \boldsymbol{\varphi}_{q-1}) \quad (\text{C.10})$$

assembles the residuals and

$$\Delta \mathbf{x} = (\Delta \tau_0^0, \Delta \mathbf{y}_1^0, \dots, \Delta \mathbf{y}_{q-1}^0) \quad (\text{C.11})$$

is the initial value shift we get in each iteration, we finally converge into the continuous solution. The speed of convergence varies with the number of sub-intervals q , which thus has to be optimized in each iteration. We typically increase q corresponding to $q \rightarrow q+4$ starting at $q=4$ until we achieve convergence. This is efficient, because it keeps q small. Note that adding only a single interval, i.e., $q \rightarrow q+1$, leads to four extra dimensions in the quadratic system $\mathbf{J} \Delta \mathbf{x} = -\mathbf{F}$.

The multiple shooting is assumed to be converged if $\|\mathbf{F}\| < \epsilon_{\text{multi}}$, which also implies $|f(\mu)| < \epsilon_{\text{multi}}$. It is thus reasonable to use $\epsilon_{\text{single}} = \epsilon_{\text{multi}}$. Note that the multiple shooting method has to be applied only if the required accuracy in the single shooting method could not be reached.

The resulting deformed shape

$$\mathbf{y}(s_0, \mathbf{x}) = \begin{pmatrix} r(s_0, \mathbf{x}) \\ z(s_0, \mathbf{x}) \\ \psi(s_0, \mathbf{x}) \\ \tau_s(s_0, \mathbf{x}) \end{pmatrix} \quad (\text{C.12})$$

is obtained as a function of the parameter set $\mathbf{x} = \{p, \nu, K_{2D}\}$, which are adapted during the shape regression (see Sec. Appendix D) to optimally match the contour points extracted from the image.

Appendix D. Shape regression

In the shape regression we find the material parameters which minimize the deviation/error between contours and theoretical shapes from solving shape equations.

The Laplace-Young equation depends on the parameter set $\mathbf{x}_0 = (p_0, \Delta\rho, \alpha)$, where α is a scaling factor, which sets the length scale. The elastic shape equations depend on the parameter set $\mathbf{x} = (p, \nu_{2D}, K_{2D})$. Let (\hat{r}_i, \hat{z}_i) with $i = 1, \dots, N$ be a set of contour points resulting from image processing. We translate this set of contour points, such that these are symmetric with respect to the z -axis and the apex is located at $z = 0$. We then accordingly chose $z(0) = \zeta = 0$. We thereby fix the theoretical shape relatively to the contour points at the apex, and minimize the residual along the remaining shape profile.

The residuals

$$\boldsymbol{\varphi}_i = \min_{s_0 \in [0, L_0]} \begin{pmatrix} |\hat{r}_i| - r(s_0, \mathbf{x}) \\ \hat{z}_i - z(s_0, \mathbf{x}) \end{pmatrix} \quad (\text{D.1})$$

are calculated by a bisection-like algorithm in the arc length s_0 , which terminates when the interval length falls below the threshold ϵ_{ms} . From the residuals $\boldsymbol{\varphi}_i$ we calculate the average mean square deviation

$$\chi = \sqrt{\frac{1}{N} \sum_{i=1}^N \|\boldsymbol{\varphi}_i\|^2} \quad (\text{D.2})$$

between the contour and the theoretical shape, as well as the Jacobians

$$\mathbf{J}_0 = \frac{\partial(\boldsymbol{\varphi}_1, \dots, \boldsymbol{\varphi}_N)}{\partial(p_0, \Delta\rho, \alpha)} \quad (\text{D.3})$$

$$\mathbf{J} = \frac{\partial(\boldsymbol{\varphi}_1, \dots, \boldsymbol{\varphi}_N)}{\partial(p_0, \nu_{2D}, K_{2D})} \quad (\text{D.4})$$

for the reference and the deformed shape. These Jacobians are sufficient to minimize the error χ and find the best fit parameter set \mathbf{x} by solving the strongly over-determined system $\mathbf{J}_F \Delta \mathbf{x} = -\mathbf{F}$ iteratively. Note that

we have to find the best fit parameter set for the reference shape first, and afterwards perform the shape regression for the deformed shape, using the already determined reference shape. Each iteration of shape regression requires three numerical derivatives to find the elements of the Jacobian, which in turn require two executions of the shooting method. This yields a parameter shift $\Delta\mathbf{x}$ in each iteration, which we assume to be converged if we find $\lambda_j\|\Delta\mathbf{x}\| < \epsilon_{\text{laplace/hooke}}$ during the backtracking line search. In addition to the minimization algorithm explained above, our software additionally provides the so-called Nelder-Mead downhill simplex method, which works without derivatives. In rare cases, where the standard procedure fails, one should try this more robust method.

Appendix E. Numerical thresholds

To ensure convergence of the shape regression and the shooting method, we have to specify thresholds.

For the average mean square displacement (D.2), i.e., the individual residuals (D.1) between the contour points and the theoretical shape we apply a bisection-like algorithm terminating when the interval length falls below the threshold ϵ_{rms} .

For the single and multiple shooting methods we define the thresholds ϵ_{single} and ϵ_{multi} , which have different meanings: the accuracy ϵ_{single} is reached if $|f| < \epsilon_{\text{single}}$, see eq. (C.1), is satisfied for the boundary deviation at the capillary, whereas the accuracy ϵ_{multi} is reached if $\|F\| < \epsilon_{\text{multi}}$ is satisfied for the global residual, which also implies $|f| < \epsilon_{\text{multi}}$. We define $\epsilon_{\text{laplace}}$ and ϵ_{hooke} as thresholds for the euclidean norm of the parameter shift $\lambda_j\Delta\mathbf{x}$, which is applied to the parameters of the shape equations during the regression and the backtracking line search, respectively. To integrate the shape equations we use a 4-th order Runge-Kutta method with constant step widths h_{laplace} and h_{hooke} .

In Tab. (Appendix E) standard values for the numerical algorithms are given. For the analysis of the capsules used in this paper, the numerical thresholds always ranged within the given boundaries. To improve the performance for specific capsules these thresholds can be increased, but it should be checked if the results are still in rough agreement with higher precision measurements, meaning that no systematic errors occur. Note that the parameters of the image processing also change the numerical behavior since the set of contour points results directly from image processing. Changing, for example, the width of the Gaussian smoothing of the image will alter the fitting results.

symbol	precision	performance
ϵ_{rms}	10^{-16}	10^{-16}
ϵ_{single}	10^{-6}	10^{-4}
ϵ_{multi}	10^{-6}	10^{-4}
$\epsilon_{\text{laplace}}$	10^{-6}	10^{-4}
ϵ_{hooke}	10^{-6}	10^{-4}
h_{laplace}	10^{-4}	10^{-3}
h_{hooke}	10^{-4}	10^{-3}

Table E.1: Precision and performance optimized values for the thresholds used in the numerical algorithms.

Appendix F. Image processing and requirements

Several filters, transformations and algorithms are applied to the image in order to get a set of contour points, which can be used for shape regression. Initially, we use a Gaussian filter to smoothen the image and run the Canny edge detection. This is common practice to extract contours from images. From the binary image we measure the outer and inner capillary diameter (the latter implicitly in terms of the fit parameter α), which is necessary to relate the length scale set in the image to SI units. Likewise, we measure the height of the capsule and its distance from the bottom of the image. These quantities are necessary to translate the contour points according to the remarks stated in Appendix D. Furthermore, we extract the contour points and reduce their number to improve efficiency. To ensure that the capturing algorithm works correctly, images have to meet certain requirements. In principle, all file formats supported by the OpenCV library can be used with our software, but we recommend png-files. Gravity should act downwards along the vertical axis and the capsule should be centered in the image with the capillary entering the image at the top. If these requirements are fulfilled, it is, in contrast to the typical pendant drop software packages, not necessary to select the capsule region manually, since the software detects the capillary and therefore the top side of the capsule automatically. The background should be uniformly colored and clean from small particles or other objects disturbing the edge detection. To ensure a proper automatic wrinkle detection the wrinkles should be visible over the whole width of the capsule. If the edge detection for the wrinkles does not work, one can provide a manually measured wrinkle wavelength in the configuration file. Even if the edge detection for the wrinkles works, one should randomly check the results by measuring the wrinkling length manually since the automatic detection requires

uniformly illuminated capsules.

- [1] H. Rehage, M. Husmann, A. Walter, From two-dimensional model networks to microcapsules, *Rheol. Acta* 41 (4) (2002) 292–306.
- [2] A. D. Dinsmore, M. F. Hsu, M. G. Nikolaidis, M. Marquez, A. R. Bausch, D. A. Weitz, Colloidosomes: selectively permeable capsules composed of colloidal particles., *Science* 298 (5595) (2002) 1006–9.
- [3] E. M. Freer, T. Svitova, C. J. Radke, The role of interfacial rheology in reservoir mixed wettability, *J. Pet. Sci. Eng.* 39 (1-2) (2003) 137–158.
- [4] B. A. Noskov, G. Loglio, R. Miller, Dilational surface viscoelasticity of polyelectrolyte/surfactant solutions: Formation of heterogeneous adsorption layers, *Adv. Colloid Interface Sci.* 168 (1-2) (2011) 179–197.
- [5] B. A. Noskov, Protein conformational transitions at the liquid-gas interface as studied by dilational surface rheology, *Adv. Colloid Interface Sci.* 206 (2014) 222–238.
- [6] E. Aumaitre, S. Knoche, P. Cicuta, D. Vella, Wrinkling in the deflation of elastic bubbles, *Eur. Phys. J. E* 36 (3) (2013) 22.
- [7] E. Donath, G. B. Sukhorukov, F. Caruso, S. A. Davis, H. Möhwald, Novel Hollow Polymer Shells by Colloid-Templated Assembly of Polyelectrolytes, *Ang. Chem. Int. Ed.* 37 (16) (1998) 2201–2205.
- [8] E. Guzman, H. Ritacco, F. Ortega, T. Svitova, C. J. Radke, R. G. Rubio, F. Ortega, T. Svitova, C. J. Radke, Adsorption Kinetics and Mechanical Properties of Ultrathin Polyelectrolyte Multilayers : Liquid-Supported versus Solid-Supported Films Adsorption Kinetics and Mechanical Properties of Ultrathin Polyelectrolyte Multilayers : Liquid-Supported versus Solid-S, *J. Phys. Chem. B* 113 (2009) 7128–7137.
- [9] A. D. Cramer, W.-F. Dong, N. L. Benbow, J. L. Webber, M. Krawowska, D. A. Beattie, J. K. Ferri, The influence of polyanion molecular weight on polyelectrolyte multilayers at surfaces: elasticity and susceptibility to saloplasticity of strongly dissociated synthetic polymers at fluidfluid interfaces, *Phys. Chem. Chem. Phys.* 19 (2017) 23781–23789.
- [10] M. P. Neubauer, M. Poehlmann, A. Fery, Microcapsule mechanics: From stability to function, *Adv. Colloid Interface Sci.* 207 (2014) 65–80.
- [11] O. I. Vinogradova, O. V. Lebedeva, B.-S. Kim, Mechanical Behavior and Characterization of Microcapsules, *Annu. Rev. Mater. Res.* 36 (1) (2006) 143–178.
- [12] J. K. Ferri, C. Kotsmar, R. Miller, From surfactant adsorption kinetics to asymmetric nanomembrane mechanics: Pendant drop experiments with subphase exchange, *Adv. Colloid Interface Sci.* 161 (1-2) (2010) 29–47.
- [13] D. Carvajal, E. J. Laprade, K. J. Henderson, K. R. Shull, Mechanics of pendant drops and axisymmetric membranes, *Soft Matter* 7 (22) (2011) 10508.
- [14] J. K. Ferri, P. A. L. Fernandes, J. T. McRuiz, F. Gambinossi, Elastic nanomembrane metrology at fluidfluid interfaces using axisymmetric drop shape analysis with anisotropic surface tensions: deviations from YoungLaplace equation, *Soft Matter* 8 (40) (2012) 10352.
- [15] P. Erni, H. A. Jerri, K. Wong, A. Parker, Interfacial viscoelasticity controls buckling, wrinkling and arrest in emulsion drops undergoing mass transfer, *Soft Matter* 8 (26) (2012) 6958–6967.
- [16] N. A. Alexandrov, K. G. Marinova, T. D. Gurkov, K. D. Danov, P. A. Kralchevsky, S. D. Stoyanov, T. B. Blijdenstein, L. N. Arnaudov, E. G. Pelan, A. Lips, Interfacial Layers from the Protein HFBII Hydrophobin: Dynamic Surface Tension, Dilatational Elasticity and Relaxation Times, *J. Colloid Interface Sci.* 376 (1) (2012) 296–306.
- [17] K. D. Danov, R. D. Stanimirova, P. A. Kralchevsky, K. G. Marinova, N. A. Alexandrov, S. D. Stoyanov, T. B. Blijdenstein, E. G. Pelan, Capillary meniscus dynamometry—method for determining the surface tension of drops and bubbles with isotropic and anisotropic surface stress distributions, *J. Colloid Interface Sci.* 440 (2015) 168–178.
- [18] A. R. Salmon, R. M. Parker, A. S. Groombridge, A. Maestro, R. J. Coulston, J. Hegemann, J. Kierfeld, O. A. Scherman, C. Abell, Microcapsule Buckling Triggered by Compression-Induced Interfacial Phase Change, *Langmuir* 32 (42) (2016) 10987–10994.
- [19] S. Knoche, D. Vella, E. Aumaitre, P. Degen, H. Rehage, P. Cicuta, J. Kierfeld, Elastometry of deflated capsules: Elastic moduli from shape and wrinkle analysis, *Langmuir* 29 (40) (2013) 12463–12471.
- [20] J. M. Andreas, E. A. Hauser, W. B. Tucker, Boundary Tension By Pendant Drops, *J. Phys. Chem.* 42 (1) (1937) 1001–1019.
- [21] C. E. Stauffer, The measurement of surface tension by the pendant drop technique, *J. Phys. Chem.* 69 (6) (1965) 1933–1938.
- [22] M. G. Cabezas, A. Bateni, J. M. Montanero, A. W. Neumann, Determination of surface tension and contact angle from the shapes of axisymmetric fluid interfaces without use of apex coordinates, *Langmuir* 22 (24) (2006) 10053–10060.
- [23] J. D. Berry, M. J. Neeson, R. R. Dagastine, D. Y. Chan, R. F. Tabor, Measurement of surface and interfacial tension using pendant drop tensiometry, *J. Colloid Interface Sci.* 454 (2015) 226–237.
- [24] S. C. Russev, N. Alexandrov, K. G. Marinova, K. D. Danov, N. D. Denkov, L. Lyutov, V. Vulchev, C. Bilke-Krause, Instrument and methods for surface dilatational rheology measurements, *Rev. Sci. Instrum.* 79 (10) (2008) 1–10.
- [25] R. Miller, J. K. Ferri, A. Javadi, J. Krägel, N. Mucic, R. Wüstneck, Rheology of interfacial layers, *Colloid Polym. Sci.* 288 (9) (2010) 937–950.
- [26] V. I. Kovalchuk, F. Ravera, L. Liggieri, G. Loglio, P. Pandolfini, A. V. Makievski, S. Vincent-Bonnieu, J. Krägel, A. Javadi, R. Miller, Capillary pressure studies under low gravity conditions, *Adv. Colloid Interface Sci.* 161 (1-2) (2010) 102–114.
- [27] L. Vaccari, D. B. Allan, N. Sharifi-Mood, A. R. Singh, R. L. Leheny, K. J. Stebe, Films of bacteria at interfaces: three stages of behaviour, *Soft Matter* 11 (30) (2015) 6062–6074.
- [28] P. Erni, P. Fischer, E. J. Windhab, V. Kusnezov, H. Stettin, J. Läger, Stress- and strain-controlled measurements of interfacial shear viscosity and viscoelasticity at liquid/liquid and gas/liquid interfaces, *Rev. Sci. Instrum.* 74 (11) (2003) 4916–4924.
- [29] I. Koleva, H. Rehage, Deformation and orientation dynamics of polysiloxane microcapsules in linear shear flow, *Soft Matter* 8 (13) (2012) 3681–3693.
- [30] G. Pieper, H. Rehage, D. Barthès-Biesel, Deformation of a capsule in a spinning drop apparatus, *J. Colloid Interface Sci.* 202 (2) (1998) 293–300.
- [31] S. Vandebril, A. Franck, G. G. Fuller, P. Moldenaers, J. Vermant, A double wall-ring geometry for interfacial shear rheometry, *Rheol. Acta* 49 (2) (2010) 131–144.
- [32] S. Reynaert, C. F. Brooks, P. Moldenaers, J. Vermant, G. G. Fuller, Analysis of the magnetic rod interfacial stress rheometer, *J. Rheol.* 52 (1) (2008) 261–285.
- [33] D. Barthès-Biesel, *Microhydrodynamics and Complex Fluids*, CRC Press, 2012.
- [34] A. Libai, J. G. Simmonds, *The Nonlinear Theory of Elastic Shells*, Cambridge University Press, 1998.
- [35] Gnu general public license.

URL <http://www.gnu.org/licenses/gpl.html>

- [36] D. Barthès-Biesel, A. Diaz, E. Dhenin, Effect of constitutive laws for two-dimensional membranes on flow-induced capsule deformation, *J. Fluid Mech.* 460 (2002) 211–222.
- [37] S. Knoche, J. Kierfeld, Buckling of spherical capsules, *Phys. Rev. E* 84 (4) (2011) 046608.
- [38] S. Le Tirilly, C. Tregouet, S. Bone, C. Geffroy, G. Fuller, N. Pantoustier, P. Perrin, C. Monteux, Interplay of hydrogen bonding and hydrophobic interactions to control the mechanical properties of polymer multilayers at the oil–water interface, *ACS Macro Lett.* 4 (1) (2014) 25–29.
- [39] J. Hegemann, J. Kierfeld, Pendant capsule elastometry. URL <https://github.com/jhegemann/opencapsule>
- [40] A. Torcello-Gómez, J. Maldonado-Valderrama, M. J. Gálvez-Ruiz, A. Martín-Rodríguez, M. A. Cabrerizo-Vílchez, J. De Vicente, Surface rheology of sorbitan tristearate and β -lactoglobulin: Shear and dilatational behavior, *J. Nonnewton. Fluid. Mech.* 166 (12) (2011) 713–722.
- [41] R. Krishnaswamy, S. Majumdar, A. Sood, Nonlinear viscoelasticity of sorbitan tristearate monolayers at liquid/gas interface, *Langmuir* 23 (26) (2007) 12951–12958.
- [42] P. Erni, P. Fischer, E. J. Windhab, Sorbitan tristearate layers at the air/water interface studied by shear and dilatational interfacial rheology, *Langmuir* 21 (23) (2005) 10555–10563.
- [43] S. Knoche, J. Kierfeld, Secondary polygonal instability of buckled spherical shells, *EPL* 106 (2) (2014) 24004.
- [44] H. Rehage, B. Achenbach, M. Geest, H. W. Siesler, Ultrathin dynamic networks formed by the surfactant span 65 at the air–water and oil–water interface, *Colloid Polym. Sci.* 279 (6) (2001) 597–606.
- [45] M. Nagel, T. A. Tervoort, J. Vermant, From drop-shape analysis to stress-fitting elastometry, *Adv. Colloid Interface Sci.* 247 (July) (2017) 33–51. doi:10.1016/j.cis.2017.07.008.
- [46] S. Knoche, J. Kierfeld, Elasticity of Interfacial Rafts of Hard Particles with Soft Shells, *Langmuir* 31 (19) (2015) 5364–5376.